

2022-01

Pleistocene depositional environments and links to cryosphere-ocean interactions on the eastern Ross Sea continental slope, Antarctica (IODP Hole U1525A).

King, M

<http://hdl.handle.net/10026.1/18063>

10.1016/j.margeo.2021.106674

Marine Geology

Elsevier

All content in PEARL is protected by copyright law. Author manuscripts are made available in accordance with publisher policies. Please cite only the published version using the details provided on the item record or document. In the absence of an open licence (e.g. Creative Commons), permissions for further reuse of content should be sought from the publisher or author.

1 ***Pleistocene depositional environments and links to cryosphere-ocean interactions on the eastern***
2 ***Ross Sea continental slope, Antarctica (IODP Hole U1525A).***

3 *Maxine V. King^{1*}, Jenny A. Gales¹, Jan Sverre Laberg², Robert M. McKay³, Laura De Santis⁴, Denise K.*
4 *Kulhanek⁵, Phillip J. Hosegood¹, Antony Morris⁶, and IODP Expedition 374 Scientists⁷*

5 *1. School of Marine and Biological Sciences, University of Plymouth, Drake Circus, Plymouth, PL4 8AA,*
6 *UK. Email: maxine.king@plymouth.ac.uk, jenny.gales@plymouth.ac.uk,*
7 *phil.hosegood@plymouth.ac.uk*

8 *2. Department of Geosciences, UIT The Arctic University of Norway, Postboks 6050 Langnes, N-9037*
9 *Tromsø, Norway. Email: jan.laberg@uit.no*

10 *3. Antarctic Research Centre, Victoria University of Wellington, PO Box 600, Wellington 6140, New*
11 *Zealand. Email: robert.mckay@vuw.ac.nz*

12 *4. National Institute of Oceanography and Applied Geophysics (OGS), Borgo Grotta Gigante, 42/c,*
13 *34010 Sgonico TS, Italy. Email: ldesantis@inogs.it*

14 *5. Institute of Geosciences, Christian-Albrechts-University of Kiel, Ludewig-Meyn-Straße 10, 24118*
15 *Kiel, Germany. Email: denise.kulhanek@ifg.uni-kiel.de*

16 *6. School of Geography, Earth and Environmental Sciences, University of Plymouth, Drake Circus,*
17 *Plymouth, PL4 8AA, UK. Email: antony.morris@plymouth.ac.uk*

18 *7. International Ocean Discovery Program/Texas A&M University, 1000 Discovery Drive, College*
19 *Station, TX 77845, USA. Email: Expedition_374_Participants@iodp.tamu.edu*

20 **Corresponding Author. Email: maxine.king@plymouth.ac.uk; Present Address: School of Marine and*
21 *Biological Sciences, Marine Building, University of Plymouth, James Street, Plymouth, Devon, PL4 6EQ*

22 ***Abstract***

23 The repeated proximity of West Antarctic Ice Sheet (WAIS) ice to the eastern Ross Sea continental
24 shelf break during past ice age cycles has been inferred to directly influence sedimentary processes
25 occurring on the continental slope, such as turbidity current and debris flow activity; thus, the
26 records of these processes can be used to study the past history of the WAIS. Ross Sea slope
27 sediments may additionally provide an archive on the history and interplay of density-driven or
28 geostrophic oceanic bottom currents with ice-sheet-driven depositional mechanisms. We investigate
29 the upper 121m of Hole U1525A, collected during International Ocean Discovery Program (IODP)
30 Expedition 374 in 2018. Hole U1525A is located on the southwestern external levee of the Hillary
31 Canyon (Ross Sea, Antarctica) and the depositional lobe of the nearby trough-mouth fan. Using core
32 descriptions, grain size analysis, and physical properties datasets, we develop a lithofacies scheme
33 that allows construction of a detailed depositional model and environmental history of past ice
34 sheet-ocean interactions at the eastern Ross Sea continental shelf break/slope since ~2.4 Ma. The
35 earliest Pleistocene interval (~2.4-~1.4 Ma) represents a hemipelagic environment dominated by ice-
36 rafting and reworking/deposition by relatively persistent bottom current activity. Finely
37 interlaminated silty muds with ice-rafted debris (IRD) layers are interpreted as contourites. Between
38 1.4 and 0.8 Ma, geostrophic bottom current activity was weaker and turbiditic processes more
39 common, likely related to the increased proximity of grounded ice at the shelf edge. Silty, normally-
40 graded laminations with sharp bases may be the result of flow-stripped turbidity currents
41 overbanking the canyon levee during periods when ice was grounded at or proximal to the shelf
42 edge. A sand, IRD- and foraminifera-bearing interval dated to ~1.18 Ma potentially reflects warmer
43 oceanographic conditions and a period of stronger Antarctic Slope Current flow. This may have
44 enhanced upwelling of warm Circumpolar Deep Water onto the shelf, leading to large-scale glacial
45 retreat at that time. The thickest interval of turbidite interlamination was deposited after ~1 Ma,
46 following the onset of the Mid-Pleistocene Transition, interpreted as a time when most ice sheets
47 grew and glacial periods were longer and more extreme. Sedimentation after 0.8Ma was dominated
48 by glacial debris flow deposition, as the trough mouth fan that dominates the eastern Ross Sea

49 continental slope prograded and expanded over the site. These findings will help to improve
50 estimations of WAIS ice extent in future Ross Sea shelf-based modelling studies, and provide a basis
51 for more detailed analysis of the inception and growth of the WAIS under distinct oceanographic
52 conditions.

53 Keywords: Eastern Ross Sea, Sedimentary process, Trough-mouth fan, Turbidites, Pleistocene

54 **1. Introduction**

55 Recent accelerated rates of ice mass loss from the West Antarctic Ice Sheet (WAIS), driven by
56 enhanced oceanic-induced melting, have demonstrated the urgent need for a refined understanding
57 of past ocean-ice sheet interactions on the Antarctic margin (Harig & Simons, 2015; Shepherd et al.,
58 2018; Rignot et al., 2019). The WAIS is generally grounded well below sea level on overdeepened
59 continental shelves, contributing towards an unstable ice sheet that is highly responsive to oceanic
60 and atmospheric variability (Hughes, 1973; Schröder et al., 2019). Recent studies show that the
61 average WAIS thinning rate continues to increase and has provided the largest contribution to
62 overall mass loss of the Antarctic Ice Sheet (AIS) since 2000 (McMillan et al., 2014; Shepherd et al.,
63 2018). The rapid nature of these losses is reflected in rising sea level and changing global climate
64 (Dangendorf et al., 2019). Furthermore, modern estimates predict oceanic-induced basal melting
65 removes approximately half of all gains in AIS surface mass before reaching the calving zone of an ice
66 shelf (Depoorter et al., 2013). This emphasises the need for improved constraints on past grounded
67 ice and oceanographic variability during periods of ice sheet growth and retreat.

68 The Ross Sea has been the subject of extensive studies to explore its glacial history, sedimentary
69 environments, and oceanographic regimes; particularly through large-scale ventures such as
70 ANTOSTRAT (Antarctic Offshore Stratigraphy Project) and ANDRILL (Antarctic Drilling Project)
71 (ANTOSTRAT, 1995; Naish et al., 2009; McKay et al., 2012). However, until recently, such studies
72 have primarily focused on collecting data from the mid continental shelf, where sequences provide

73 direct records of ice sheet advance but preserve a highly discontinuous record due to glacial
74 overriding. Consequently, investigating the sedimentary mechanisms operating on the Ross Sea
75 continental slope over time can help to decode regional oceanographic change, and also provide a
76 valuable stratigraphic connection to discontinuous shelf records of ice shelf variability that are
77 subject to the erosive action of grounded ice (Barker et al., 1999; Barker & Camerlenghi, 2002;
78 Rebesco et al., 2006). Interpretation of sedimentary sequences from this region of the Antarctic
79 continental margin may also help to understand complex interactions between along- and down-
80 slope processes, which are further complicated by Coriolis-driven offset (Kuvaas et al., 2005;
81 Rebesco et al. 2007; Salles et al., 2010; Alonso et al., 2016; Miramontes et al., 2020).

82 We use sediments collected during International Ocean Discovery Program (IODP) Expedition 374 to
83 provide a detailed description of the depositional environment on the eastern Ross Sea continental
84 slope during the Pleistocene. This will help to improve interpretations of grounded ice activity on the
85 continental shelf, and investigate changes in regional-scale oceanographic features (e.g. downslope
86 flow of dense water from sea ice production on the shelf; along-slope flow of bottom currents) that
87 may be linked to changing ice cover on the continental shelf. Using these data, we aim to
88 understand: 1) the processes that operated on the eastern Ross Sea upper slope, Antarctica, during
89 the Pleistocene; 2) the characteristics, timing and frequency of these processes and 3) how they
90 relate to glacial/interglacial cycles. The palaeo-sedimentary signature of these processes may reveal
91 important information regarding regional palaeo-ice sheet dynamics and the wider behaviour of the
92 WAIS in response to climate forcing.

93 ***1.1. Regional Setting***

94 IODP Site U1525 was drilled in 2018 and is located on the upper continental slope in the eastern
95 Ross Sea, Antarctica, ~60km northeast of the continental shelf break at 1776m water depth
96 (75°0.06'S, 173°55.20'W; Fig. 1) (McKay et al., 2019b). Site U1525 lies on the gently-sloping flank of

97 an asymmetric sediment mound on the continental slope that forms part of the southwestern
98 external levee of the Hillary Canyon, to the southeast of the Iselin Bank (McKay et al., 2019b).

99 In the Eastern Ross Sea, ice drains through fast ice streams from the WAIS, calving at the modern-
100 day ice front of the Ross Ice Shelf roughly 350-375km landward from the continental shelf break
101 (Anderson et al., 1984; Bart, 2004). Along this section of the margin, the Glomar Challenger and
102 Pennell Troughs bisect the shelf break, which are thought to be the location of palaeo-ice streams
103 during past glacial periods (Cooper et al., 1991; De Santis et al., 1995; Shipp et al., 1999). Deeply-
104 incised gully and channel systems are potentially related to canyon head processes in the Hillary
105 Canyon (Gales et al., 2021). A prograding trough-mouth fan (TMF) system lies to the east of the
106 canyon (Fig. 1a-b and Fig. F24 in McKay et al., 2019b) (Alonso et al., 1992). High input of glacial
107 sediments through these troughs during glacial periods were likely responsible for the formation of
108 this fan.

109 A number of seismic and sedimentological studies conducted in the Ross Sea have revealed several
110 periods of glacial advance and retreat over the Pleistocene, including instances where WAIS ice was
111 grounded at the continental shelf break during pronounced glacial periods such as the last glacial
112 maximum (LGM) (Anderson et al., 1984; De Santis et al., 1999; Bart, 2004; Mosola & Anderson,
113 2006; Bart & Owolana, 2012; Halberstadt et al., 2016; Prothro et al., 2018). Strong seismic reflectors,
114 known as the Ross Sea seismic unconformities (RSU1-6), record the major ice sheet grounding
115 events since the Oligocene (RSU6; ~30Ma) (De Santis et al., 1999). An R/V OGS Explora cruise funded
116 by the Antarctic Italian Program “Programma Nazionale delle Ricerche in Antartide” collected
117 seismic reflection data in 1994 from across Site U1525 (Fig. 1c), which showed the presence of such
118 reflectors on the slope that have been interpreted as RSU2-4 (4-2.5 Ma, 10-5.5 Ma and ~15.8-14.6
119 Ma respectively) (Brancolini et al., 1995; McKay et al., 2019b; Conte et al., 2021). These data also
120 show a ~1km-thick sequence of mostly high to medium amplitude, parallel and internally stratified
121 reflectors indicative of sediment drifts, and the overspill and flow-stripping deposits of turbidity

122 currents on the slope. The uppermost seismic unit of the TMF shows acoustically-transparent or
123 chaotic deposits consistent with glacial debris flows above RSU2, burying sediment drifts and
124 channel-levees in the continental slope (Fig. 1c), and suggesting major progradation of the fan
125 during the late Pliocene/early Pleistocene (4.0-2.5 Ma) in response to changing glacial dynamics
126 (Lindeque et al., 2016; Kim et al., 2018; Conte et al., 2021). Volumetric-based assessments of
127 grounding-zone wedges in the Glomar Challenger Trough suggest grounding line advance over the
128 last glacial cycle may have been as rapid as 13m/yr; although this value is not a precise measure, it
129 illustrates the potential for dynamic WAIS behaviour in the Ross Sea (Bart & Owolana, 2012).

130 Oceanographically, the Hillary Canyon is a significant location in the Ross Sea for dense shelf water
131 overflow into the deep ocean, which mixes with Modified Circumpolar Deep Water to form Antarctic
132 Bottom Water (Bergamasco et al., 2002; Budillon et al., 2002; Whitworth & Orsi, 2006; Budillon et
133 al., 2011). Down-slope flows of dense shelf water are deflected westward due to the Coriolis force
134 (Morrison et al., 2020). A westward-flowing component of the Antarctic Slope Current (ASC) has also
135 been identified in the eastern Ross Sea, which is a possible contributor to the external canyon
136 levee's asymmetrical structure (Orsi & Wiederwohl, 2009; Miramontes et al., 2020).

137 **2. Methods**

138 **2.1. Data collection and shipboard physical properties measurements**

139 IODP Hole U1525A was cored to a depth of 208.28 metres below seafloor (mbsf) through Plio-
140 Pleistocene sediments. Here we focus on the interval between 0-121.04 mbsf, which was selected to
141 provide a representative view of changing palaeoenvironmental conditions at Site U1525 across the
142 Pleistocene. Coring primarily used the advanced piston corer and half-length advanced piston corer,
143 although the extended core barrel was also used to drill through over-compacted sediments
144 between 43-55.7 mbsf (McKay et al., 2019a). Cores were scanned on-board for magnetic
145 susceptibility (pass-through and point-source), gamma-ray attenuation (GRA) bulk density and
146 natural gamma radiation (NGR). High-resolution core images were taken using a line-scan camera

147 (20 pixels/mm). Discrete $\sim 10\text{cm}^3$ sediment samples were extracted at approximately 75cm intervals
148 for the purposes of calculating grain density and porosity. Unless otherwise specified, the core depth
149 below sea floor method A(CSF-A) depth scale is reported here as mbsf. Detailed information on the
150 methods used during Expedition 374 can be found in McKay et al. (2019a).

151 **2.2. Grain size analysis**

152 Grain size analyses for 0-121.05 mbsf were conducted using a Malvern Mastersizer 2000 laser
153 particle size-analyser with an autosampler. Four subsamples of approximately 8mm^3 (approx. 0.1g)
154 of sediment were dry sieved through a 1mm mesh, treated with a 10% H_2O_2 solution to remove
155 organic material and placed in a water bath at 60°C overnight to assist the reaction process. A 10%
156 solution of sodium hexametaphosphate was added to the Mastersizer wet sample dispersion unit
157 and 40 seconds of ultrasound was applied to disperse material before measurement. Samples were
158 analysed using an absorption coefficient of 0.005 and refractive index of 1.53. Coarse material was
159 then manually dry-sieved in a nested stack at half-phi intervals (between 1.4-63mm). Ice-rafted
160 debris (IRD) was characterised as material larger than 1mm in diameter, unless the unit was
161 subsequently identified as a mass flow. The grain size boundaries used for clay, silt and sand in the
162 laser particle size analysis are $<4\mu\text{m}$ (clay), $63\mu\text{m}$ (silt) and $63\text{-}1000\mu\text{m}$ (very fine-coarse sand),
163 respectively. The classification scheme used for sediment nomenclature and colour can be found in
164 McKay et al. (2019a). The term 'mud' is used as a descriptor for sediments with a mixture of silt and
165 clay where neither size class dominates (i.e. $<80\%$ silt, or $<80\%$ clay) as per the sediment
166 nomenclature scheme.

167 **2.3. Laminae analysis**

168 Laminae were classified into two categories on the basis of visual observations (e.g. thickness, colour
169 and boundary characteristics), which are referred to as 'Type A' and 'Type B' (see Table 1 and section
170 3.3 for descriptions of laminae types). Grain size was not used as an identification factor as analyses

171 showed both types of laminae are predominantly coarse silts. Measurements were taken from the
172 core midpoint at the base of the lamina to the nearest millimetre. Type B laminae 'packages' were
173 counted as single laminae due to the fine-scale nature and discontinuity of laminae enclosed within
174 (section 3.3).

175 **2.4. Age Model**

176 We use the shipboard age model for Site U1525 that uses magnetic reversal stratigraphy, supported
177 by biostratigraphic datums from published Southern Ocean zonations (Fig. 2) (McKay et al., 2019a).
178 These utilised the first appearance and last appearance datum of marine diatom and radiolarian
179 species. Palaeomagnetic reversals were correlated to the Gradstein et al. (2012) geomagnetic
180 polarity timescale, which are calibrated using marine magnetic anomaly profiles (Hilgen et al., 2012;
181 Lourens et al., 2004). The interval of Unit III discussed in this paper (118.58-121.05 mbsf; ~2.4Ma)
182 and Subunits IIA/B are early-mid Pleistocene (~2.4 Ma to ~0.8 Ma). Unit I is of mid-Late Pleistocene
183 age (<~0.8Ma). The shipboard age model includes two interpreted unconformities. Unconformity 1
184 (U1) is present within the interval of no recovery between 38.83 and 55.7 mbsf. Drilling parameters
185 were used to determine when the bit penetrated the base of the over-compacted sediments and
186 suggest that the unconformity is likely present near the base of this interval (McKay et al., 2019b).
187 Unconformity 2 (U2) is present near the base of the studied interval at ~112 mbsf. The thickness of
188 Unit I is fully constrained, however the base of the unit was not piston-cored due to the presence of
189 consolidated or coarse material in the sequence. Drilling parameters (e.g. rate of penetration,
190 weight on bit) infer that Unit I exists down to ~55.7 mbsf, as piston coring was able to resume only
191 after these parameters indicate sediments were soft enough to penetrate with a piston core. This is
192 unlike U2, which is not well constrained in the depth domain but is thought to cover a longer time
193 interval than U1 (~1.95-2.4 Ma; McKay et al., 2019b).

194 **3. Results**

195 **3.1. Core Overview**

196 We refine the preliminary lithofacies classification scheme from McKay et al., 2019b into seven
197 lithofacies, which are summarised in Table 1 and Figures 2-3, and described in more detail in the
198 Supplementary Information. We describe these seven lithofacies in the context of the three primary
199 lithostratigraphic units that were identified during initial shipboard core analysis (McKay et al.,
200 2019b). Unit I (0-51.11 mbsf), Unit II (51.11-118.58 mbsf), which is further divided into Subunits IIA
201 and IIB, and Unit III (118.58-208.27 mbsf/base of hole). The boundary between Subunit IIA and IIB is
202 located at 98.2 mbsf (Figs. 2, 3). The principal lithologies identified in this core are diamict and mud.

203 **3.2. Unit I Facies**

204 Unit I contains muddy diamict and is mostly grey, diatom-bearing, unconsolidated and massive, here
205 referred to as facies MDm, with a ~2m-thick interval of stiff and weakly stratified muddy diamict
206 facies MDs between 15.28-17.64 mbsf (Fig. 2, Table 1). Grain size analyses of the two facies in Unit I
207 reveal similar matrix particle size distributions, both of which are also distinctly richer in gravel and
208 sand than the underlying units (Figs. 4, 5a/b/c). Both facies in Unit I show percentages of average
209 mud (silt and clay; 55%wt) sand (32%wt) and gravel (13%wt) content comparable to diamicts
210 recovered from other Antarctic TMFs, such as on the Belgica and Weddell Sea slopes (Melles, 1991;
211 Hillenbrand et al., 2009a; Gales et al., 2018). The percentage of clay is mostly uniform in Unit I
212 (average 18% of <1mm fraction), as most of the variation in grain size is seen in the percentage of silt
213 and sand (Fig. 2). Facies MDs is very stiff and is similar to stratified diamicts recovered from the
214 Prydz Bay TMF (Passchier et al., 2003). The matrix is also slightly sandier than in facies MDm, and it
215 also contains a number of larger sub-angular to sub-rounded clasts (Figs. 2, 4, 5c).

216 **3.3. Unit II Facies**

217 Unit II is located below U1 and contains a strikingly different lithology to Unit I. Sediments are
218 composed of mostly greenish-grey, massive to laminated diatom-bearing/rich muds. Unit II also
219 contains a higher and more variable amount of clay (average 25% of <1mm fraction) than Unit I, and

220 is rich in post-depositional soft sediment deformation features such as cm-scale micro-faulting, as
221 well as cm-scale diamicts and matrix-supported gravel layers (Table 1; Figs. 6, 7, 8). Magnetic
222 susceptibility, bulk density and NGR show lower average values than in Unit I (Fig. 2). Five facies in
223 Unit II have been identified in this study: mud with 'Type A' silt laminae and dispersed clasts, Ms(A)
224 (Figs. 6a/b, 7b, 8); massive mud, Mm (Figs. 6c, 7a); interbedded diatom-bearing muddy
225 diamict/sandy mud and foraminifera-bearing clast-rich sandy diamict, SDi (Fig. 6d); and mud with
226 'Type B' silt laminae, gravel layers and dispersed clasts, Ms(B) (Figs. 7c/d, 8). Gravel in these layers is
227 mostly angular to sub-rounded and between 1mm - 4mm in diameter, with occasional larger clasts
228 up to 11mm in size.'

229 **3.3.1. Type A' Lamina- facies Ms(A)**

230 Type A laminae are planar, normally graded and have sharp lower contacts that show truncation of
231 underlying sediments (Fig. 9). In facies Ms(A), there are two main modes of Type A lamination: a)
232 Mode 1: strongly interlaminated mud with silt laminae, and b) Mode 2: faintly-laminated mud
233 interbedded with cm-scale sandy muds or muddy diamicts (Table 1; Figs. 6a/b, 7b, 8). Laminae in
234 interlaminated intervals are rarely thicker than 1-2 mm, evenly spaced (1-5 mm) and usually
235 decrease in frequency toward the upper and lower limits of the interlaminated intervals. The
236 majority of sampled Type A laminae are coarse silts, but are occasionally very fine-grained sand in
237 the rarer, thicker lamina (>1cm; Figs. 4, 8). Clasts are rarely found within strongly laminated intervals
238 (Mode 1) but are more common in the muddier sections of Mode 2.

239 **3.3.2. 'Type B' Laminae- facies Ms(B)**

240 Silty Type B laminae in this interval are characteristically distinct from those in facies Ms(A) and
241 exhibit sharp upper and lower contacts with no grading (Fig. 9). Furthermore, gravel layers and
242 dispersed clasts are common between instances of Type B laminae. Many laminae are exceptionally
243 thin (1-2mm), although very fine, stacked, mm-scale discontinuous laminae form packages up to 1

244 cm thick (Fig. 8). Similarly to facies Ms(A), facies Ms(B) is composed of a) Mode 1: more strongly-
245 laminated intervals and b) Mode 2: areas of less frequent lamination that commonly shows slight to
246 heavy bioturbation (Table 1, Fig. 2). Matrix-supported, gravel-rich layers are common in both modes
247 of this facies, ranging in thicknesses from 1mm-1cm and with mostly gradational, occasionally sharp
248 lower contacts.

249 **3.4. Unit III Facies**

250 The 2.47 m of Unit III between 118.58-121.05 mbsf included in this study is assigned to facies MDi,
251 which is diatom-rich, cm- to dm-scale diamict interbedded with muds containing dispersed clasts
252 and silt/gravel laminae (Figs. 10a/b, 11). It contains average clay values (23% of <1mm fraction)
253 similar to Unit II (Fig. 2). The boundary between Unit II and III does not appear to be accompanied by
254 a stratigraphic unconformity, with U2 occurring slightly above this lithostratigraphic boundary at
255 ~112 mbsf (McKay et al., 2019b). Gravel in layers is mostly angular to sub-rounded and between
256 1mm - 4mm in diameter, with occasional larger clasts up to 11mm in size.

257 **3.5. Frequency Analysis**

258 Three main diamict units are observed in Unit I, corresponding to changes in physical properties and
259 visual characteristics, which are illustrated in Figure 12 along with the frequency occurrence of Type
260 A and B laminations. These diamicts are variable in thickness and in clast content. The thickest
261 deposit, interval D1, is homogenous and displays little evidence of containing separate deposits.
262 Interval D2 corresponds to the stiff diamict facies MDs, and interval D3 sits directly above U1.
263 Diamicts in Unit II and III are thinner and separated from one another by several metres of other
264 sediment types. The most distinct Unit II diamict is interval D6 (facies SDi), interbedded between
265 muddy diatom-bearing diamict/sandy muds and foraminifer-bearing sandy diamicts. Most diamicts
266 in units II and III are found in the diatom-rich Subunits IIB and Unit III (intervals D8-12), whereas the

267 two main deposits in Subunit IIA (intervals D4-5) directly succeed thin, diatom-rich mud intervals
268 (Figs. 2, 12).

269 Laminated sediments show distinct, high-frequency intervals of both Type A and Type B laminae
270 occurring in a waxing-waning pattern (Fig. 12). Type A laminae (normally-graded silt or very fine sand
271 laminae with erosive bases) are present throughout all of Unit II, whereas Type B (silt laminae with
272 sharp upper and lower contacts, no grading) are found in Subunit IIB and III. Type A laminae are
273 found primarily in Subunit IIA but are also weakly present in Subunit IIB after intervals of Type B
274 lamination (Figs. 2, 12). Type B laminae are concentrated within five main intervals and display some
275 of the highest frequencies of laminae in the core (33 laminae/10 cm). Some higher frequency
276 intervals appear to succeed thin diamict intervals D8-10. Type B high frequency intervals between
277 ~105-118 mbsf are also followed by short, low frequency intervals of Type A laminae.

278 Type A laminae are concentrated into 4 main intervals above ~95 mbsf, and mostly show greater
279 spacing between high-frequency intervals than peaks in Type B laminae frequency. Type A
280 interlaminated intervals are therefore thicker than interlaminated intervals of Type B. The thickest
281 interlaminated interval in U1525A is found between ~57-64 mbsf, which lies between interval D4
282 and U1.

283 **4. Facies Interpretation**

284 **4.1. Facies MDm**

285 Facies MDm (D1, D3) are interpreted here as glacial debris flows due to their size, lithological
286 structure, high clast content and matrix grain size distribution. The occurrence of these deposits in
287 Hole U1525A are indicative of upper slope failure driven by ice grounded at the continental shelf
288 break as inferred for other high-latitude margins (e.g. Laberg & Vorren, 1996; Vorren & Laberg,
289 1997; Tripsanas & Piper, 2008). Periods of intense ice-rafting and the subsequent rainout of
290 entrained IRD may also deposit diamict on polar continental slopes; however, these deposits are

291 often thin, stratified, texturally heterogeneous, and possess gradational contacts (Kurtz & Anderson,
292 1979). Furthermore, the lack of microfossils in MDm could suggest that source sediments were likely
293 deposited close to or further inland of the grounding line, away from open marine conditions
294 favourable to biological activity (Anderson et al., 1984; Licht et al., 1999; Prothro et al., 2018). This
295 would discount ice-rafting as the sole process responsible for coarse material in Unit I. Facies MDm
296 displays characteristics (soft, massive, muddy diamict) similar to glacial debris flow deposits
297 identified on other Antarctic continental margins, such as in the Bellingshausen and Weddell Seas
298 (Kurtz & Anderson, 1979; King et al., 1998; Passchier et al., 2003; Hillenbrand et al., 2009a; Gales et
299 al., 2018). Soft diamicts may develop primarily on the outer shelf in a number of depositional
300 settings, such as deformed subglacial diamicts, grounding line-proximal diamicts, and iceberg-
301 turbated diamicts (Domack et al., 1990; Licht et al., 1999). Sediment cores from Deep Sea Drilling
302 Project (DSDP) Sites 270, 271 and 272 extracted from the Glomar Challenger Trough reveal a ~19 m-
303 long microfossil-barren Pleistocene sub-unit of 'sand-silt-clay with pebbles', Unit 1B, which includes
304 a significant fraction (<20%wt) of sand (Fig.1; Barrett, 1975). The textural characteristics of DSDP-
305 270-272 Unit 1B are reflected in the bimodal muddy-sand matrix of diamicts in Hole U1525A Unit I,
306 indicating that facies MDm sediments likely originated on the shelf and were reworked through
307 mass-wasting downslope (Fig.4).

308 **4.2. Facies MDs**

309 Similarly to MDm, facies MDs (D2) is interpreted to be the result of a debris flow event following the
310 delivery of large volumes of sediment to the continental shelf edge. However, the unique
311 characteristics of facies MDs (extremely stiff, low porosity, browner colour, slightly sandier matrix,
312 increased clast size range and content) indicate that the associated mass flow possessed different
313 rheological properties to those in facies MDm, and/or was subject to transformative processes after
314 deposition on the slope. The browner colour of facies MDs could indicate a change in clay
315 mineralogy or iron oxide minerals (e.g. hematite) as it does not coincide with changes in biogenic

316 content, has a high magnetic susceptibility and higher values of NGR (Wei et al., 2014). Clay minerals
317 possess diverse properties affecting sediment dilatancy, cohesion, compaction and sediment yield
318 stress, which is the minimum shear stress required to initiate flow (Hampton, 1975; Mulder et al.,
319 1997; Yu et al., 2013). This change in sediment colour may be an indicator of variable sediment
320 source input (Andrews & Jennings, 1987). Sediment entrainment within the basal shear zone may be
321 the cause of reduced clast size and content towards the lowermost ~15 cm of the facies (Lowe,
322 1982; Laberg & Vorren, 2000). Thus, weak stratification probably occurred during the debris flow
323 event as a result of surface substrate deformation and not from depositional and/or erosional
324 processes on the continental shelf.

325 **4.3. Facies Ms(A)**

326 We interpret Type A laminae in facies Ms(A) as low-density turbidity current deposits mobilised on
327 the upper slope of the Hillary Canyon, following facies models of fine-grained turbidites (Lowe, 1982;
328 Stow & Piper, 1984; Shanmugam, 1997). Turbidites with similar characteristics (barren, IRD-sparse,
329 interlaminated mud containing normally-graded silt or very fine sand laminae with erosive bases;
330 Fig. 9) have been documented at several locations around the Antarctic continental margin,
331 indicating rapid deposition of sediments under energetic seabed conditions (Pudsey, 2000, 2002;
332 Lucchi et al., 2002; Lucchi & Rebesco, 2007; Cowan et al., 2008; Caburlotto et al., 2010). Grain size
333 spectra of Type A laminae (Fig. 8) show low concentrations of sand and characteristic modes in the
334 medium-coarse silt fraction that are similar to deposits created by overbank spilling of turbidity
335 currents identified on the Labrador Sea slope (Chough & Hesse, 1980; Wang & Hesse, 1996) and the
336 Pacific margin of the Antarctic Peninsula (Lucchi et al., 2002). High frequency intervals of Type A
337 laminae may therefore represent overbank deposits from turbidity currents that have spilt over the
338 crest of the external Hillary Canyon levee during glacial periods (Fig. 13). Overbanking is a process
339 that is likely restricted to the inner flank and crest of the external levee (Piper & Normark, 1983;
340 Peakall et al., 2000). Therefore, given Site U1525's location on the outer flank of the external canyon

341 levee, Type A laminae may be the settled remains of fine-grained sediment that have been flow-
342 stripped from turbidity currents mobilised on the inner levee flank (Peakall et al., 2000; Sinclair &
343 Tomasso, 2002).

344 Low-density turbidity currents may have deposited sediment rapidly enough to account for the lack
345 of distinct IRD packages and bioturbation in Type A interlaminated intervals (Wang & Hesse, 1996;
346 Lucchi et al., 2002; Lucchi et al., 2013). This may explain why gravel in Mode 1 of facies Ms(A) is rare
347 and dispersed (Table 1). Furthermore, grounded ice terminating at the shelf break, as well as other
348 small fringing ice shelves, are likely to have released comparatively 'cleaner' icebergs containing less
349 entrained debris in comparison with inland outlet glaciers only exposed to ocean calving during
350 interglacial periods (Smith et al., 2019). The four main episodes of high turbidity current activity
351 recorded in Subunit IIA may therefore reflect the incidence of subglacial sediment release at the
352 shelf break in this section of the eastern Ross Sea. Peaks in turbidite (Type A) frequency found prior
353 to ~1.1 Ma are closer together and shorter in sequence, whereas the large peak after ~1.1 Ma
354 suggests a much more prolonged period of turbidity current deposition (Figs. 2, 12).

355 In facies Ms(A) Mode 2, the grey muddy diamicts (intervals D4-5, 9)/sandy muds with sharp upper
356 contacts were likely deposited as glacimarine diamict resulting from increased glacial calving and
357 retreat and subjected to winnowing. This is in line with interpretations of IRD-rich hemipelagic
358 sediments from other Antarctic continental margins (Pudsey, 2000, 2002; Passchier et al., 2003;
359 Lucchi & Rebesco, 2007; Caburlotto et al., 2010; Patterson et al., 2014).

360 **4.4. Facies Mm**

361 Facies Mm is interpreted as interglacial sediment deposited through hemipelagic processes,
362 including rainout of fine-grained terrigenous material suspended in the water column. The
363 characteristics of facies Mm (greenish grey, lacking bioturbation and rare IRD) are not typical of
364 interglacial sediments, which are usually identified as bioturbated, sandy muds that are browner in

365 colour and contain IRD (Wang & Hesse, 1996; Pudsey, 2002; Hillenbrand et al., 2009b; Passchier et
366 al., 2011; Patterson et al., 2014;). Evidence of warmer oceanographic conditions or increased
367 productivity in these interglacial sediments is not clearly reflected in microfossil content (i.e., no
368 obvious change in % diatoms, foraminifera or calcareous nanofossils; Fig. 2). This suggests that,
369 during interglacial periods, biological material was not preserved in the fossil record due to their
370 composition; for example, algae such as *Phaeocystis* do not produce fossil remains (Goffart et al.,
371 2000), or it was removed prior to or following deposition through physical and/or chemical
372 processes, e.g. test dissolution due to a shallow carbonate compensation depth (Fillon, 1975).
373 Plumite mud beds with characteristics similar to facies Mm (structureless or some faint colour
374 contrasts with no textural variation, sparse IRD and lacking bioturbation) are observed on the
375 eastern Prydz Bay margin, East Antarctica, and the Antarctic Peninsula (Pudsey & Camerlenghi, 1998;
376 Passchier et al., 2003; Lucchi & Rebesco, 2007). However, pure plumite facies may have a seaward
377 limit of no more than tens of kilometres from the ice margin on the shelf and are attributed to
378 meltwater plume release from glacial advance or retreat (Hesse et al., 1997; Lucchi et al., 2002).

379 **4.5. Facies SDi**

380 Facies SDi (interval D6; Fig. 12) is unique in Hole U1525A and is here interpreted as possible evidence
381 of glacial collapse, based on the presence of planktonic foraminifera and high amounts of sand and
382 gravel (Figs. 2, 4). A diverse benthic assemblage was also found in this facies (McKay et al., 2019b).
383 Foraminifera in Ross Sea sedimentary sequences are usually indicative of sea-ice free, open marine
384 interglacial conditions, as planktonic species are relatively sparse in the continental shelf waters and
385 increase in abundance seawards on the slope and rise (Majewski et al., 2018). The coarse grain size
386 of facies SDi may be a joint result of rapid emplacement of IRD and increased bottom current
387 velocity. Strongly interlaminated turbidite intervals (Mode 1 of Facies Ms(A), described in section
388 3.3.1) are also missing in facies SDi, providing further evidence of the absence of proximal grounded
389 ice (Fig. 2). The diatom-bearing muddy diamict/sandy mud intervals interbedded between each

390 foraminifera-bearing sandy deposit could suggest that glacial collapse occurred in a series of large-
391 scale calving events that were punctuated by brief periods of glacial re-advance.

392 **4.6. Facies Ms(B)**

393 Silty Type B laminae found in Unit III and Subunit IIB are interpreted as deposits influenced by
394 geostrophic current activity. The characteristics of Type B laminae (<2mm thickness, sharp upper and
395 lower contacts, no grading; Fig. 9), along with the presence of dispersed clasts and gravelly IRD
396 layers in the diatom-rich facies Ms(B), reflect previous descriptions of muddy glacial contourites
397 (Piper & Brisco, 1975; Pudsey, 2000; Lucchi & Rebesco, 2007; Passchier et al., 2011). Grain size
398 distributions for muds in facies Ms(B) display a dominant mode at $\sim 7.8 \mu\text{m}$ (Figs. 4, 8), whereas Type
399 B laminae are slightly coarser at $\sim 10\text{-}11 \mu\text{m}$. Together with the laminae characteristics (horizontal,
400 wispy and fine-grained) and other sedimentary structures (i.e. thicker laminae 'packages'), these
401 lithological features suggest an alternating but relatively low to moderate current strength where
402 deposition dominates over winnowing (Pudsey, 2000; Rebesco et al., 2014). Evidence of deposition
403 under a lower-energy environment in facies Ms(B) is further supported by the presence of laminae
404 draping over clasts and minor bioturbation (Fig. 8; Sup. Info), although sediments mostly lack
405 bioturbation. Minimal bioturbation may explain why Type B laminated intervals in facies Ms(B)
406 Mode 1 are relatively well-preserved, particularly in laminae 'packages'. This is in agreement with
407 laminated contourites found in sediment drifts off the Pacific margin of the Antarctic Peninsula,
408 where Lucchi & Rebesco (2007) suggested that climatically influenced reductions in deep water
409 oxygenation, and a longer seasonal duration of sea-ice cover into the summer months act to
410 suppress primary productivity, explaining the lack of bioturbation. Type B laminations in Subunit IIB
411 show larger peaks in frequency towards the base of the unit, reflecting a more prolonged period of
412 bottom current activity before $\sim 1.7\text{Ma}$ (Fig. 12). The on/off style of Type B lamination frequency
413 potentially relates to changing bottom current intensity over time, with peaks in frequency
414 representing periods of time where current speed increased (Stow et al., 2002; Lucchi & Rebesco,

415 2007). Gravel/IRD layers show an episodic input of IRD in Subunit IIB, suggesting pulse-like delivery
416 of IRD to the site (Fig. 8). Bioturbated diamicts in Ms(B) Mode 2 (D7-8) are also consistent with IRD-
417 rainout and resemble intervals D4-5 (section 4.3). As the large quantity of IRD layers deviate from
418 the 'end-member' description of glacial contourites, facies Ms(B) is probably a hybrid deposit
419 resulting from sustained bottom current activity coupled with hemipelagic settlement of IRD and
420 fine-grained sediments suspended in the water column.

421 **4.7. Facies MDi**

422 Coarse sand and gravel in Facies MDi are interpreted as IRD deposited by a mixture of slow,
423 sustained rainout from calved icebergs (sparse IRD) and large pulses of IRD delivery (IRD-rich layers)
424 from increased melting and grounded ice retreat. This interpretation is in alignment with IRD
425 deposits identified from Scoresby Sund, East Greenland, and the Antarctic Peninsula (Dowdeswell et
426 al., 1994; Lucchi et al., 2002). Muddy intervals and weak laminae are also present in this facies,
427 although in much thinner stratigraphic intervals, suggesting that similar along-slope processes
428 responsible for facies Ms(B) also operated to deposit facies MDi. Bioturbated, inversely-graded
429 diamicts interbedded with weakly-laminated mud in this facies (D10-12) suggests deposition in a
430 hemipelagic environment with strong influence from IRD rainout. D10-D12 are therefore interpreted
431 as possible gravel-lag deposits winnowed by periodic strengthening of bottom currents as described
432 in Stow et al. (2002) and Rebesco et al. (2014).

433 **5. Discussion**

434 **5.1. Along-slope influenced processes (Units II and III)**

435 Regional interpretations of seismic and seabed bathymetry data have shown large sediment drifts
436 building on the Hillary Canyon external levees (Fig. 1c), with seabed morphology indicating that
437 strong northwest-flowing bottom currents exist (De Santis et al., 1999; De Santis et al., 2015; Kim et
438 al., 2018; McKay et al., 2019b; Conte et al., 2021). The presence of contourites is supported by

439 modern in-situ oceanographic observations from the western flank of the Hillary Canyon that shows
440 down- and along-slope bottom currents with velocities of up to 15 cm s^{-1} (Jacobs et al., 1970;
441 Bergamasco et al., 2002; Orsi & Wiederwohl, 2009; Budillon et al., 2011). Given that bottom current-
442 influenced facies Ms(B) was likely deposited under low current speeds, Site U1525 may have been
443 exposed to weak along-slope bottom current flow during the early Pleistocene, rather than to higher
444 current velocities. This is consistent with modern oceanographic measurements suggesting that the
445 greatest current velocities in the Hillary Canyon are currently focussed higher on the upper slope
446 (Budillon et al., 2011). Variations in the along-slope current speed that are potentially responsible
447 for the on/off style of Type B lamination could relate to changes in the strength and/or location of
448 the along-slope current core (Rebesco et al., 2014), which is supported by evidence of variable
449 along-slope current speeds and contourite deposition on the Iselin Bank since the late Miocene
450 (Conte et al., 2021). Instability of along-slope currents likely resulted from movement of the ice front
451 through glacial-interglacial cycles and/or shifting patterns of Westerly winds. Within muddy intervals
452 such as facies Mm (Subunit IIA/B), which can extend up to 3.0 m thick in sequence, the absence of
453 strong interlamination could imply prolonged periods of reduced geostrophic and gravity-driven
454 bottom current activity during interglacial periods.

455 At Site U1525, benthic activity may have been inhibited due to reduced ventilation of shelf waters,
456 as sea ice reduced vertical mixing of deep ocean water masses such as Circumpolar Deep Water
457 (CDW) (Patterson et al., 2014; Stein et al., 2020). Low concentrations of benthic foraminifera and
458 other microfossils associated with strengthened ventilation and upwelling, or open-marine
459 conditions, in facies Mm and Ms(B) supports this; however, it should be noted that the modern
460 calcite compensation depth in the Ross Sea is shallow ($\leq 430\text{m}$), which inhibits the preservation of
461 calcareous foraminifera (Kennett, 1968). The presence of microfossil-barren glacial contourite facies
462 Ms(B) therefore may imply the influence of longer duration seasonal sea-ice into the summer
463 months, and subsequent restricted ventilation of shelf water masses that feed oxygenated bottom
464 water to Site U1525.

465 Suspended fine-grained material originating from other canyon systems to the southeast (e.g.
466 Whales Deep & Little America Basins, Fig. 1a-b) may have been laterally advected to the site via
467 weak along-slope currents and Coriolis forcing, potentially delivering sediment from several sources
468 on the shelf. For example, meltwater plumes entrained in currents may travel up to ~130km away
469 from their source (Hesse et al., 1997). Furthermore, nepheloid layers are common on the Ross Sea
470 margin and have been observed at water depths exceeding 1500 m below sea level around the
471 Hillary Canyon (Jacobs et al., 1970; Budillon et al., 2006; Capello et al., 2009). Settlement from re-
472 suspended fine-grained glacial marine sediment discharge at the grounding line therefore likely
473 supplied much of the fine-grained sediment at Site U1525 in Units II-III. These processes may have
474 also remained relevant into the late Pleistocene, however sediments in Unit I are anticipated to have
475 undergone significant reworking. The early Pleistocene (~2.4 Ma to ~1.4 Ma; Subunit IIB/ Unit III)
476 depositional environment at Site U1525 is therefore envisaged to be a greater function of reworking
477 by the along-slope bottom current component, rather than gravity-driven bottom currents or mass
478 wasting. However, the original sediment supply to these water depths prior to bottom current
479 reworking may have been driven by downslope processes.

480 ***5.2. Down-slope influenced processes (Unit II)***

481 Turbidity currents deposits found in Mode 1 of facies Ms(A) were probably initiated by sediment
482 loading on the upper slope from the release of subglacial debris, as well as sediment-laden subglacial
483 meltwater, from the base of margin-proximal and retreating grounded ice on the shelf (e.g. Ó
484 Cofaigh et al., 2003; Noormets et al., 2009). Evidence for extensive turbidity current activity exists in
485 deeply-incised gully systems along the shelf edge at the Hillary Canyon head, which were likely
486 formed over multiple glacial cycles by erosive turbidity currents (Gales et al., 2021). Considering the
487 location of Site U1525 on the canyon flank (Fig. 1), the absence of high-energy sedimentary features
488 e.g. cross-stratification or rip-up clasts in facies Ms(A), could suggest that the main body of turbidity
489 currents were centred in the Hillary Canyon. This hypothesis is supported by seismic interpretations

490 of contourite drifts from the western flank of the Hillary Canyon suggesting that the formation of the
491 canyon levees occurred prior to the Pleistocene (McKay et al., 2019b; Conte et al., 2021).

492 After ~1.4Ma (Subunit IIA and above) where facies Ms(A) is most common, the preservation of
493 turbidites suggest that bottom current reworking ceased or significantly decreased. Flow-stripping
494 could also explain why Type A laminae are less abundant in Subunit IIB, as fine-grained sediment
495 suspended via flow-stripping could have been winnowed away from the site as a combined result of
496 stronger geostrophic current activity enhanced by Coriolis forcing (Wang & Hesse, 1996). This may
497 exclude a secondary hypothesis for Type B interlamination as a product of gravity-driven and along-
498 slope processes acting contemporaneously, as is observed on many polar continental margins
499 (Kuvaas & Leitchenkov 1992; Michels et al., 2001; Rebesco et al., 2007; Mulder et al., 2008). The
500 waxing-waning style of Type B laminae peaks are similar to Type A, which could suggest they are the
501 remains of turbidity currents winnowed by stronger along-slope bottom currents (Andersen et al.,
502 1996; Escutia et al., 2000, 2003). Whilst we anticipate that a complex interplay of processes
503 contributed towards sedimentation in most, if not all facies in Hole U1525A, our interpretation of
504 Type A laminae as deposits from turbidity currents initiated when ice was more proximal to the shelf
505 break contradicts this hypothesis.

506 Turbidity currents initiated as a result of margin-proximal ice depositing sediment at the shelf break
507 do not explain the presence of weak, less frequent (<10 laminae/10cm) and discontinuous Type A
508 laminae in the 2.4 to 1.4 Ma (Subunit IIB) interval of Hole U1525A, which occur after peaks in Type B
509 laminations (Fig. 12). Site U1525 was likely located north of the Ross Sea TMF during the early
510 Pleistocene, until the TMF prograded over the core site (see section 5.4). Hence, some turbidites
511 may also represent the distal portion of debris flows operating on the TMF as flow transformation
512 occurs via the progressive entrainment of water into the debris flow body over distance (Fisher,
513 1983; Stow, 1985; Stow & Smillie, 2020). The lack of turbidite interlamination (facies Ms(A) Mode 1;
514 Table 1), and lack of debris flow deposits in Subunit IIB suggest that episodes of grounded ice

515 advance to the shelf break, if they occurred, were either significantly reduced in a) frequency and/or
516 b) duration of fully-extended conditions (Fig. 12). Periodic WAIS advances are documented in AND-
517 1B across all of the Plio-Pleistocene (Naish et al., 2009), although these data from Hole U1525A
518 suggest that very few of these advances likely reached the shelf break. When the WAIS was not
519 under full glacial conditions, turbidity currents may also have been triggered by other mechanisms,
520 such as cascading dense shelf water or slope failure relating to isostatic rebound processes;
521 however, the relationship between sediment gravity flows and cascades is not well defined (Figs. 2,
522 11) (Bart et al., 1999; Canals et al., 2006). Gravity-driven overflows of dense shelf water cascade over
523 the shelf break in highly localised regions such as the Hillary Canyon, as well as passively in smaller
524 submarine canyons along the eastern Ross Sea margin (Amblas & Dowdeswell, 2018; Bergamasco et
525 al., 2002; Jacobs, 1991; Jacobs & Haines, 1982). High amounts of cascading dense shelf water,
526 turbidity currents, and hyperpycnal flows at the mouths of other canyon systems along the margin
527 (including the Hillary Canyon) could contribute towards the resuspension of fine sediments and
528 maintenance of a nepheloid layer (Escutia et al., 2000, 2005; De Santis et al., 2003; Donda et al.,
529 2003). Persistent, intense periods of dense shelf water cascading could mobilise low-density
530 sediment gravity flows on the Hillary Canyon slope, if sediment were able to accumulate on the
531 slope over extended periods of time (Gales et al., 2021). However, the modern oceanographic
532 setting shows that the Coriolis force drives dense shelf water to cascade further towards the
533 western area of the Hillary Canyon (Budillon et al., 2011; Morrison et al., 2020; Gales et al., 2021).
534 Assuming this was also the case during the early-mid Pleistocene, and that slope/shelf break
535 palaeobathymetry did not impede along-slope current activity in the Hillary Canyon, turbidity
536 currents resulting from cascading may therefore not have occurred close enough to the core site to
537 influence sedimentation to a significant degree at Site U1525. Consequently, a sedimentary
538 sequence covering the same time interval drilled on the opposite canyon flank is anticipated to differ
539 from the sequence recorded at Site U1525, possibly to a great extent.

540 The increased frequency of Type A interlamination after ~1 Ma is likely due to a prolonged grounded
541 ice presence at the margin during the Mid-Pleistocene Transition (MPT; ~1 Ma), interpreted as a
542 time when most ice sheets, including the WAIS, increased in size, covering longer, asymmetrical 100
543 kyr glacial/interglacial cycles rather than the obliquity-forced, symmetrical 41 kyr cycles seen
544 previously (Tziperman & Gildor, 2003; Lisiecki & Raymo, 2005; Naish et al., 2009; Pollard & DeConto,
545 2009).

546 ***5.3. Ice Rafted Debris (Units II and III)***

547 Icebergs calving into the eastern Ross Sea are typically deflected westwards with wind and surface
548 water current direction (Keys & Fowler, 1989), supplying IRD from multiple locations along the ice
549 front in the Ross Sea and also potentially from further to the east. The gravel-rich intervals D4-12
550 found in Mode 2 of facies Ms(A)/Ms(B) and facies MDi that are interpreted as periods of sustained
551 IRD deposition during deglacial periods therefore likely contain IRD from several bedrock source
552 regions. IRD-sparse interglacial facies Mm may highlight changing iceberg pathways, possibly relating
553 to reduced transport from further east by the ASC or polynyas near the shelf break acting to divert
554 icebergs away from the core site during interglacials. However, current and iceberg drift patterns
555 would mostly be regulated by palaeobathymetry and the ASC. Alternatively, it could indicate relative
556 stability of the ice sheet margin during these periods if the transference of heat and fresh water
557 through water mass exchange across the shelf break was also stable (Lucchi et al., 2002; Budillon et
558 al., 2011).

559 ***5.4. Glacially-induced debris flows (Unit I)***

560 The three main diamict intervals identified in Unit I (D1-3; facies MDm and MDs) may reflect the
561 frequency occurrence of debris flows at the site, however more work is needed to constrain this
562 further (Fig. 12). Due to the location of Site U1525 on the upper slope, debris flows of sufficient size
563 and erosional capacity likely entrained the uppermost layer of sediment, bypassing and
564 redistributing deglacial and interglacial sediments towards the outer margins of the fan and the

565 continental rise (Laberg & Vorren, 2000). This accounts for the lack of contouritic deposits,
566 turbidites, or hemipelagic deposits usually associated with sedimentation on TMFs between full
567 glacial periods (Vorren & Laberg, 1997). The shift to glacigenic debris flow-dominated sedimentation
568 is a probable result of continued TMF progradation across the gently-sloping flank of the Hillary
569 Canyon external levee, in response to the increased delivery of subglacial material to the shelf break
570 and aided by gravitational settling from subglacial meltwater plumes (Fig. 13). Delivery and melt-out
571 of subglacial debris by ice sheet advance to the shelf edge, alongside sediment-laden subglacial
572 meltwater release likely contributed towards the continued progradation of the TMF (Tripsanas &
573 Piper, 2008; Lucchi et al., 2013).

574 Diamicts across the Ross Sea continental shelf show consistency in matrix grain size despite variable
575 bedrock sources (Perotti et al., 2017; Halberstadt et al., 2018), therefore increased influence of ice-
576 rafting could explain why more sand is present in the sediment matrix of facies MDs without an
577 associated reduction in clay. Before remobilisation, diamict temporarily stored on the upper slope as
578 a glacial wedge by grounded ice at the margin may have had a longer residence time prior to slope
579 failure (Laberg & Vorren, 1995), and was subsequently subjected to a greater influence of
580 glacimarine or ice-rafted deposition. It is therefore also conceivable that facies MDs is the result of
581 changing grounded ice-stream dynamics delivering sediments from differing upstream bedrock
582 sources. Ice flow switching occurred in the Ross Sea in response to variations in East and West
583 Antarctic Ice Sheet dynamics, and drainage changes on other WAIS-controlled continental shelves
584 have occurred during the late Quaternary (Mosola & Anderson, 2006; Hillenbrand et al., 2009b;
585 Greenwood et al., 2012). Terminal moraines on the Eastern Ross Sea shelf have also shown a pre-
586 LGM grounding event that displays a major shift in WAIS ice stream direction from west to north
587 (Bart, 2004; Böhm et al., 2009). Further investigation of clast and clay mineral provenance could
588 provide useful insight into the origin of facies MDs.

589 ***5.5. Further considerations: results from other Antarctic marine drill cores***

590 ***5.5.1. Early Pleistocene (Marine Isotope Stage 31, ~1.1 Ma)***

591 The variety of species within the benthic assemblage in facies SDi points towards changing bottom
592 water conditions, with winnowing of smaller planktonic tests (<250µm) implying strengthened
593 bottom current speeds possibly related to intensified wind-driven along-slope flow of the ASC
594 (McKay et al., 2019b). This enhanced ASC flow may have allowed more intrusions of relatively warm,
595 nutrient-rich CDW further onto the Ross Sea continental shelf through Ekman pumping, reducing sea
596 ice production due to heat supply, enhancing basal melt in the ice shelf cavity and providing more
597 favourable biological conditions (Anderson et al., 1984; Morrison et al., 2020). Diatomite in AND-1B
598 and a carbonate-rich unit from Cape Roberts Project drill core CRP-1, both dated to Marine Isotope
599 Stage 31 (MIS 31) age (1.1 Ma), reflect warmer-than present, sea-ice free oceanographic conditions
600 and increased carbonate preservation in the western Ross Sea (Scherer et al., 2008; Naish et al.,
601 2009; McKay et al., 2012; Villa et al., 2012; Teitler et al., 2015). Similar carbonate-rich beds have
602 been identified at IODP Sites U1359 and U1361 from the Wilkes Land margin (Escutia et al., 2011;
603 McKay et al., 2011; Beltran et al., 2020), and from ODP Sites 1165-1167 in Prydz Bay (Villa et al.,
604 2008). This suggests that the drivers for the depositional anomaly of facies SDi in Hole U1525A occur
605 in adjacent sectors of the Antarctic margin and are not a result of a localised process. Modelling
606 studies informed by Ross Sea shelf drill core interpretations have shown an almost complete
607 collapse of the WAIS occurred during MIS 31 and earlier Pleistocene interglacials, which would have
608 translated into high calving rates and the subsequent release of large amounts of IRD into the Ross
609 Sea (DeConto et al., 2012).

610 ***5.5.2. The Mid-Pleistocene Transition and the following period (<1Ma)***

611 Our interpretation of increased turbidity current deposition at Site U1525 relating to enhanced ice
612 cover on the continental shelf after ~1 Ma is supported by AND-1B facies that suggest MIS 31 was
613 the last clear evidence of WAIS retreat and open water conditions at AND-1B. After ~1 Ma, the AND-
614 1B core is dominated by subglacial diamictites during glacial maxima, and thin mudstone units
615 during interglacials (McKay et al., 2009; 2012). This was interpreted as a baseline shift in climate

616 state across the MPT whereby ocean temperatures cooled enough to allow large ice shelves to
617 persist through interglacial periods (McKay et al., 2012), which in turn promoted ice sheet stability
618 through the buttressing effect provided by ice shelves (Weertman, 1974). Subglacial deformation
619 features in the diamictites from AND-1B indicate grounded ice sheets expanded into the Ross Sea
620 during the glacial maxima of the past 0.8 Ma. It should also be noted that no turbidite beds are
621 found in the C1n.1n subchron (Jaramillo) in Hole U1525A (Fig. 2), which coincides with the last well-
622 constrained evidence of WAIS collapse at AND-1B (Naish et al., 2009).

623 **6. Conclusions**

624 We identified seven facies using grain size and facies analysis of sediment cores collected from Hole
625 U1525A in the eastern Ross Sea. These facies correspond to differing depositional mechanisms
626 affected by oceanographic conditions and grounded WAIS dynamics on the continental shelf (Table
627 1) (McKay et al., 2019b). They also provide insight into the relative contributions of processes
628 occurring in the Hillary Canyon and the Ross Sea TMF to the depositional environment on this sector
629 of the slope. The Pleistocene (<~2.4Ma) sedimentary sequence at Site U1525 can therefore be
630 divided into three key intervals:

- 631 • Early Pleistocene (~2.4 Ma to ~1.4Ma) Units III and Subunit IIB: IRD-and diatom-rich, slightly
632 bioturbated facies with fine-scale 'Type B' interlamination, which are interpreted as
633 contourites formed by along-slope bottom current winnowing, suggesting a higher influence
634 of bottom currents at Site U1525 during the early Pleistocene relative to later time intervals.
635 Lateral advection of fine-grained sediments by along-slope bottom currents and Coriolis
636 forcing likely delivered sediments from other canyon systems further to the East of the site.
637 Interglacial sediments are characteristically lacking in bioturbation and microfossils.
- 638 • Early-mid Pleistocene (~1.4 Ma to ~0.8 Ma) Subunit IIA: 'Type A' laminations are interpreted
639 as flow-stripped turbidity current deposits focussed in the Hillary Canyon. Strongly
640 interlaminated turbidite intervals are suggested to form as high amounts of subglacial debris
641 and sediment-laden subglacial meltwater released from a proximal grounding line are

642 deposited and contribute towards slope instability. Other processes, such as cascading
643 dense shelf water or isostatic rebound, may have initiated turbidity currents outside of
644 glacial periods. A distinct sandy interval containing large amounts of ice-rafted material and
645 foraminifera-rich layers indicates open marine conditions around $\sim 1.18\text{Ma}$, a depositional
646 anomaly that is also noted in mid-Pleistocene interglacials of Wilkes Land and Prydz Bay
647 regions (Villa et al., 2008; Escutia et al., 2011; Beltran et al., 2020). This could reflect a period
648 of enhanced ASC flow towards the continental shelf, which led to strengthened inflow of
649 CDW and periodic glacial collapse during the mid-Pleistocene (1.18-1.0 Ma). The largest
650 interval of turbidite lamination occurs after $\sim 1\text{Ma}$, consistent with more prolonged/frequent
651 grounded ice presence at the shelf break leading into the MPT.

- 652 • Mid-late Pleistocene ($<0.8\text{Ma}$) Unit I: Onset of glacial debris flow sedimentation on this
653 sector of the upper slope, developing from large volumes of subglacial diamict and IRD
654 delivered to the margin. A slightly sandier and more clast-rich stiff diamict facies potentially
655 reflects variable clay mineralogy and a longer residence time on the upper slope before
656 remobilisation. Debris flows possessed sufficient erosional capacity to remove the previous
657 interglacial sequence. Colder conditions and frequent fully-extended glacial conditions
658 allowed the continued progradation of the TMF across the core site.

659 Our conceptual model derived from a semi-continuous continental slope record in the eastern Ross
660 Sea identifies increasing frequency of glacial advances to the shelf edge as a result of increased
661 Antarctic cooling over the Pleistocene, particularly after the MPT. We also identify that during
662 periods of reduced ice sheet extent of the early- to mid-Pleistocene, the depositional setting is
663 characterised by contouritic currents that we hypothesise represent a stronger ASC and enhanced
664 upwelling of warm sub-surface CDW onto the continental shelf. This led to increased frequency and
665 extent of ice sheet retreat at that time. The results presented here form a strong basis for future
666 work, where testing of these hypotheses based on the physical properties of the sediment can be
667 conducted by geochemical and palaeontological proxies at Site U1525 and other IODP Expedition

668 374 sites (U1523 and U1524). Such an approach will allow us to identify how shifts in current speed
669 and sediment delivery to the continental shelf break more directly relates to shifting surface and
670 deep water mass properties through the Plio-Pleistocene. These data will help provide fundamental
671 new insights into how oceanic processes near Antarctica's continental shelf edge have contributed
672 to the triggering of past marine-based ice sheet retreat. This work also provides valuable context for
673 regional seismic interpretations and in-depth studies of the Ross Sea TMF formation.

674 **Acknowledgements**

675 This research used samples and data provided by the International Ocean Discovery Program (IODP).
676 We thank the members of IODP Expedition 374 Science Party and the captain and crew of the
677 *JOIDES Resolution*. JSL acknowledges the support from European Consortium for Ocean Research
678 Drilling and the Research Council of Norway allowing for his participation on Expedition 374 and the
679 post-cruise work. RMM was funded by the Royal Society of New Zealand Te Apārangi Marsden Fund
680 (grant 18-VUW-089) and the NZ MBIE funded Antarctic Science Platform (ANTA1801). JG was funded
681 by the Natural Environment Research Council (grant NE/R018189/1). LD was funded by the Italian
682 Antarctic Research Program PNRA16_00016 project. DKK was funded by US National Science
683 Foundation (grants OCE-1326927 and OPP-2000995). All Expedition 374 shipboard datasets are
684 publicly available via the following link: <https://web.iodp.tamu.edu/OVERVIEW/>. The multichannel
685 seismic profile reprocessed by Riccardo Geletti (OGS) for the IODP Exp. 374 and used in this work is
686 available at the Antarctic Seismic Data Library System (<https://sdls.ogs.trieste.it>) under the auspices
687 of the Scientific Committee on Antarctic Research (SCAR) policy.

688 **References**

689 Alonso, B. A., J. B.; Díaz, J. I.; Bartek, L. R. (1992). Pliocene-Pleistocene Seismic Stratigraphy of the Ross
690 Sea: Evidence for Multiple Ice Sheet Grounding Episodes. In D. H. Elliot (Ed.), *Contributions to Antarctic*
691 *Research III* (Vol. 57, pp. 93-103).

692 Alonso, B., Ercilla, G., Casas, D., Stow, D. A. V., Rodríguez-Tovar, F. J., Dorador, J., & Hernández-Molina, F.-
693 J. (2016). Contourite vs gravity-flow deposits of the Pleistocene Faro Drift (Gulf of Cadiz):
694 Sedimentological and mineralogical approaches. *Marine Geology*, 377, 77-94.
695 doi:10.1016/j.margeo.2015.12.016

696 Amblas, D., & Dowdeswell, J. A. (2018). Physiographic influences on dense shelf-water cascading down
697 the Antarctic continental slope. *Earth-Science Reviews*, 185, 887-900.
698 doi:10.1016/j.earscirev.2018.07.014

699 Andersen, E. S., Dokken, T. M., Elverhøi, A., Solheim, A., & Fossen, I. (1996). Late quaternary
700 sedimentation and glacial history of the western Svalbard continental margin. *Marine Geology*, 133(3),
701 123-156. doi:[10.1016/0025-3227\(96\)00022-9](https://doi.org/10.1016/0025-3227(96)00022-9)

702 Anderson, J. B., Brake, C. F. and Myers, N. C. (1984). Sedimentation on the Ross Sea Continental Shelf,
703 Antarctica. *Marine Geology*, 57, 295-333. doi:10.1016/0025-3227(84)90203-2

704 Andrews, J. T., & Jennings, A. E. (1987). Influence of sediment source and type on the magnetic
705 susceptibility of fiord and shelf deposits, Baffin Island and Baffin Bay, NWT. *Canadian Journal of Earth*
706 *Sciences*, 24(7), 1386-1401. doi:10.1139/e87-131

707 ANTOSTRAT. (1995). Seismic stratigraphic atlas of the Ross Sea. *Geology and Seismic Stratigraphy of the*
708 *Antarctic Margin*, 68.

709 Arndt, J. E., Schenke, H. W., Jakobsson, M., Nitsche, F.-O., Buys, G., Goleby, B., Rebesco, M., Bohoyo, F.,
710 Hong, J. K., Black, J., Greku, R. K., Udintsev, G. B., Barrios, F., Reynoso-Peralta, W., Taisei, M., & Wigley, R.
711 (2013). *The International Bathymetric Chart of the Southern Ocean (IBCSO) - digital bathymetric model*.
712 doi:10.1594/PANGAEA.805734

713 Barker, P. F., Barrett, P. J., Cooper, A. K., & Huybrechts, P. (1999). Antarctic glacial history from numerical
714 models and continental margin sediments. *Palaeogeography, Palaeoclimatology, Palaeoecology*, 150(3),
715 247-267. doi:10.1016/S0031-0182(98)00224-7

716 Barker, P. F., & Camerlenghi, A. (2002). Glacial History of the Antarctic Peninsula from Pacific Margin
717 Sediments. *Proc. ODP, Sci. Results*, 178, 1-40. doi:10.2973/odp.proc.sr.178.238.2002

718 Barrett, P. J. (1975). Textural characteristics of Cenozoic preglacial and glacial sediments at Site 270, Ross
719 Sea, Antarctica. *Initial Reports of the Deep Sea Drilling Project*, 28, 757-767.
720 doi:10.2973/dsdp.proc.28.1975

721 Bart, P. J. (2004). West-directed flow of the West Antarctic Ice Sheet across Eastern Basin, Ross Sea
722 during the Quaternary. *Earth and Planetary Science Letters*, 228(3-4), 425-438.
723 doi:10.1016/j.epsl.2004.10.014

724 Bart, P. J., De Batist, M., & Jokat, W. (1999). Interglacial collapse of Cray Trough-mouth fan, Weddell Sea,
725 Antarctica; implications for Antarctic glacial history. *Journal of Sedimentary Research*, 69(6), 1276-1289.
726 doi:10.2110/jsr.69.1276

727 Bart, P. J., & Owolana, B. (2012). On the duration of West Antarctic Ice Sheet grounding events in Ross
728 Sea during the Quaternary. *Quaternary Science Reviews*, 47, 101-115.
729 doi:10.1016/j.quascirev.2012.04.023

730 Beltran, C., Golledge, N. R., Ohneiser, C., Kowalewski, D. E., Sicre, M.-A., Hageman, K. J., Smith, R., Wilson,
731 G. S., & Mainié, F. (2020). Southern Ocean temperature records and ice-sheet models demonstrate rapid
732 Antarctic ice sheet retreat under low atmospheric CO₂ during Marine Isotope Stage 31. *Quaternary
733 Science Reviews*, 228, 106069. doi:10.1016/j.quascirev.2019.106069

734 Bergamasco, A., Defendi, V., Zambianchi, E., & Spezie, G. (2002). Evidence of dense water overflow on the
735 Ross Sea shelf-break. *Antarctic Science*, 14(3), 271-277. doi:10.1017/S0954102002000068

736 Böhm, G., Ocañoğlu, N., Picotti, S., & De Santis, L. (2009). West Antarctic Ice Sheet evolution: New insights
737 from a seismic tomographic 3D depth model in the Eastern Ross Sea (Antarctica). *Marine Geology*,
738 266(1), 109-128. doi:10.1016/j.margeo.2009.07.016

739 Brancolini, G., Busetto, M., Marchetti, A., Santis, L., Zanolla, C., Cooper, A., Cochrane, G., Zayatz, I.,
740 Belyaev, V., Knyazev, M., Vinnikovskaya, O., & Hinz, F. (1995). Descriptive text for the seismic
741 stratigraphic atlas of the Ross Sea, Antarctica. In (pp. 271-286).

742 Budillon, G., Castagno, P., Aliani, S., Spezie, G., & Padman, L. (2011). Thermohaline variability and
743 Antarctic bottom water formation at the Ross Sea shelf break. *Deep-Sea Research Part I-Oceanographic*
744 *Research Papers*, 58(10), 1002-1018. doi:10.1016/j.dsr.2011.07.002

745 Budillon, G., Gremes-Cordero, S., & Salusti, E. (2002). On the dense water spreading off the Ross Sea shelf
746 (Southern Ocean). *Journal of Marine Systems*, 35(3-4), 207-227. doi:10.1016/s0924-7963(02)00082-9

747 Budillon, G., Salusti, E., & Tucci, S. (2006). The evolution of density currents and nepheloid bottom layers
748 in the Ross Sea (Antarctica). *Journal of Marine Research*, 64(4), 517-540.
749 doi:10.1357/002224006778715739

750 Caburlotto, A., Lucchi, R. G., De Santis, L., Macrì, P., & Tolotti, R. (2010). Sedimentary processes on the
751 Wilkes Land continental rise reflect changes in glacial dynamic and bottom water flow. *International*
752 *Journal of Earth Sciences*, 99(4), 909-926. doi:10.1007/s00531-009-0422-8

753 Canals, M., Puig, P., de Madron, X. D., Heussner, S., Palanques, A., & Fabres, J. (2006). Flushing submarine
754 canyons. *Nature*, 444(7117), 354-357. doi:10.1038/nature05271

755 Capello, M., Budillon, G., Cutroneo, L., & Tucci, S. (2009). The nepheloid bottom layer and water masses
756 at the shelf break of the western Ross Sea. *Deep Sea Research Part II: Topical Studies in Oceanography*,
757 56(13-14), 843-858. doi:10.1016/j.dsr2.2008.10.032

758 Chough, S., & Hesse, R. (1980). The Northwest Atlantic Mid-Ocean Channel of the Labrador Sea; III, Head
759 spill vs. body spill deposits from turbidity currents on natural levees. *Journal of Sedimentary Research*,
760 50(1), 227-234. doi:10.1306/212F79B4-2B24-11D7-8648000102C1865D

761 Conte, R., Rebesco, M., De Santis, L., Colleoni, F., Bensi, M., Bergamasco, A., Kovacevic, V., Gales, J., Zgur,
762 F., Accettella, D., De Steur, L., Ursella, L., McKay, R., Kim, S., & Lucchi, R. G. (2021). Bottom current control

763 on sediment deposition between the Iselin bank and the Hillary canyon (Antarctica) since the late
764 Miocene: An integrated seismic- oceanographic approach. *Deep Sea Research Part I: Oceanographic*
765 *Research Papers*, 103606. doi:[10.1016/j.dsr.2021.103606](https://doi.org/10.1016/j.dsr.2021.103606)

766 Cooper, A. K., Barrett, P. J., Hinz, K., Traube, V., Letichenkov, G., & Stagg, H. M. J. (1991). Cenozoic
767 prograding sequences of the Antarctic continental margin: a record of glacio-eustatic and tectonic events.
768 *Marine Geology*, 102(1), 175-213. doi:10.1016/0025-3227(91)90008-R

769 Cowan, E. A., Hillenbrand, C. D., Hassler, L. E., & Ake, M. T. (2008). Coarse-grained terrigenous sediment
770 deposition on continental rise drifts: A record of Plio-Pleistocene glaciation on the Antarctic Peninsula.
771 *Palaeogeography, Palaeoclimatology, Palaeoecology*, 265(3), 275-291. doi:10.1016/j.palaeo.2008.03.010

772 Dangendorf, S., Hay, C., Calafat, F. M., Marcos, M., Piecuch, C. G., Berk, K., & Jensen, J. (2019). Persistent
773 acceleration in global sea-level rise since the 1960s. *Nature Climate Change*, 9(9), 705-710.
774 doi:10.1038/s41558-019-0531-8

775 De Santis, L., Anderson, J. B., Brancolini, G., & Zayatz, I. (1995). Seismic record of late Oligocene through
776 Miocene glaciation on the central and eastern continental shelf of the Ross Sea. *Geology and Seismic*
777 *Stratigraphy of the Antarctic Margin*, 68, 235-260. doi:10.1029/AR068p0235

778 De Santis, L., Bergamasco, A., Colizza, E., Geletti, R., Accaino, F., Wardell, N., Olivo, E., Petronio, L.,
779 Henrys, S. A., Black, J., Mckay, R. M., & Bohm, G. (2015). *The Hillary Canyon and the Iselin Bank (Eastern*
780 *Ross Sea, Antarctica): Alongslope and Downslope Route For Ross Sea Bottom Water*. Paper presented at
781 the AGU Fall Meeting Abstracts. <https://ui.adsabs.harvard.edu/abs/2015AGUFMEP13A0919D>

782 De Santis, L., Brancolini, G., & Donda, F. (2003). Seismo-stratigraphic analysis of the Wilkes Land
783 continental margin (East Antarctica): influence of glacially driven processes on the Cenozoic deposition.
784 *Deep Sea Research Part II: Topical Studies in Oceanography*, 50(8), 1563-1594. doi:[10.1016/S0967-](https://doi.org/10.1016/S0967-0645(03)00079-1)
785 [0645\(03\)00079-1](https://doi.org/10.1016/S0967-0645(03)00079-1)

786 De Santis, L., Prato, S., Brancolini, G., Lovo, M., & Torelli, L. (1999). The Eastern Ross Sea continental shelf
787 during the Cenozoic: implications for the West Antarctic ice sheet development. *Global and Planetary*
788 *Change*, 23(1), 173-196. doi:10.1016/S0921-8181(99)00056-9

789 DeConto, R. M., Pollard, D., & Kowalewski, D. (2012). Reprint of: Modeling Antarctic ice sheet and climate
790 variations during Marine Isotope Stage 31. *Global and Planetary Change*, 96-97, 181-188.
791 doi:10.1016/j.gloplacha.2012.05.018

792 Depoorter, M. A., Bamber, J. L., Griggs, J. A., Lenaerts, J. T. M., Ligtenberg, S. R. M., van den Broeke, M. R.,
793 & Moholdt, G. (2013). Calving fluxes and basal melt rates of Antarctic ice shelves. *Nature*, 502(7469), 89-
794 92. doi:10.1038/nature12567

795 Domack, E. W. (1990). Laminated terrigenous sediments from the Antarctic Peninsula: the role of
796 subglacial and marine processes. *Geological Society, London, Special Publications*, 53(1), 91-103.
797 doi:10.1144/gsl.Sp.1990.053.01.05

798 Donda, F., Brancolini, G., Santis, L. D., & Trincardi, F. (2003). Seismic facies and sedimentary processes on
799 the continental rise off Wilkes Land (East Antarctica): evidence of bottom current activity. *Deep Sea*
800 *Research Part II: Topical Studies in Oceanography*, 50(8), 1509-1527. doi:[10.1016/S0967-0645\(03\)00075-4](https://doi.org/10.1016/S0967-0645(03)00075-4)

801 Dowdeswell, J. A., Whittington, R. J., & Marienfeld, P. (1994). The origin of massive diamicton facies by
802 iceberg rafting and scouring, Scoresby Sund, East Greenland. *Sedimentology*, 41(1), 21-35.
803 doi:10.1111/j.1365-3091.1994.tb01390.x

804 Escutia, C., Brinkhuis, H., & Klaus, A. (2011). IODP expedition 318: From greenhouse to icehouse at the
805 Wilkes Land Antarctic Margin. *Scientific drilling: reports on deep earth sampling and monitoring*, 12, 15-
806 23. doi:10.1016/B978-0-444-62617-2.00012-8

807 Escutia, C., De Santis, L., Donda, F., Dunbar, R. B., Cooper, A. K., Brancolini, G., & Eittrheim, S. L. (2005).
808 Cenozoic ice sheet history from East Antarctic Wilkes Land continental margin sediments. *Global and*
809 *Planetary Change*, 45(1), 51-81. doi:[10.1016/j.gloplacha.2004.09.010](https://doi.org/10.1016/j.gloplacha.2004.09.010)

810 Escutia, C., Eitrem, S. L., Cooper, A. K., & Nelson, C. H. (2000). Morphology and Acoustic Character of the
811 Antarctic Wilkes Land Turbidite Systems: Ice-Sheet-Sourced Versus River-Sourced Fans. *Journal of*
812 *Sedimentary Research*, 70(1), 84-93. doi:10.1306/2DC40900-0E47-11D7-8643000102C1865D

813 Escutia, C., Warnke, D., Acton, G. D., Barcena, A., Burckle, L., Canals, M., & Frazee, C. S. (2003). Sediment
814 distribution and sedimentary processes across the Antarctic Wilkes Land margin during the Quaternary.
815 *Deep Sea Research Part II: Topical Studies in Oceanography*, 50(8), 1481-1508. doi:[10.1016/S0967-](https://doi.org/10.1016/S0967-0645(03)00073-0)
816 [0645\(03\)00073-0](https://doi.org/10.1016/S0967-0645(03)00073-0)

817 Fillon, R. H. (1975). Late Cenozoic Paleo-Oceanography of the Ross Sea, Antarctica. *GSA Bulletin*, 86(6),
818 839-845. doi:10.1130/0016-7606(1975)86<839:Lcpotr>2.0.Co;2

819 Fisher, R. V. (1983). Flow transformations in sediment gravity flows. *Geology*, 11(5), 273-274.
820 doi:10.1130/0091-7613(1983)11<273:Ftisgf>2.0.Co;2

821 Gales, J., Rebesco, M., De Santis, L., Bergamasco, A., Colleoni, F., Kim, S., Accettella, D., Kovacevic, V., Liu,
822 Y., Olivo, E., Colizza, E., Florindo-Lopez, C., Zgur, F., & McKay, R. (2021). Role of dense shelf water in the
823 development of Antarctic submarine canyon morphology. *Geomorphology*, 372, 107453.
824 doi:10.1016/j.geomorph.2020.107453

825 Gales, J. A., Hillenbrand, C. D., Larter, R. D., Laberg, J. S., Melles, M., Benetti, S., & Passchier, S. (2018).
826 Processes influencing differences in Arctic and Antarctic trough mouth fan sedimentology. *Geological*
827 *Society, London, Special Publications*, 475, SP475.477. doi:10.1144/sp475.7

828 Goffart, A., Catalano, G., & Hecq, J. H. (2000). Factors controlling the distribution of diatoms and
829 Phaeocystis in the Ross Sea. *Journal of Marine Systems*, 27(1), 161-175. doi:10.1016/S0924-
830 7963(00)00065-8

831 Gradstein, F. M., Ogg, J. G., Schmitz, M., & Ogg, G. (2012). *The geologic time scale 2012*: Elsevier.

832 Greenwood, S. L., Gyllencreutz, R., Jakobsson, M., & Anderson, J. B. (2012). Ice-flow switching and
833 East/West Antarctic Ice Sheet roles in glaciation of the western Ross Sea. *GSA Bulletin*, *124*(11-12), 1736-
834 1749. doi:10.1130/b30643.1

835 Halberstadt, A. R. W., Simkins, L. M., Greenwood, S. L., & Anderson, J. B. (2016). Past ice-sheet behaviour:
836 retreat scenarios and changing controls in the Ross Sea, Antarctica. *Cryosphere*, *10*(3), 1003-1020.
837 doi:10.5194/tc-10-1003-2016

838 Halberstadt, A. R. W., Simkins, L. M., Anderson, J. B., Prothro, L. O., & Bart, P. J. (2018). Characteristics of
839 the deforming bed: till properties on the deglaciated Antarctic continental shelf. *Journal of Glaciology*,
840 *64*(248), 1014-1027. doi:10.1017/jog.2018.92

841 Hampton, M. (1975). Competence of fine-grained debris flows. *Journal of Sedimentary Research*, *45*(4),
842 834-844. doi:10.1306/212f6e5b-2b24-11d7-8648000102c1865d

843 Harig, C., & Simons, F. J. (2015). Accelerated West Antarctic ice mass loss continues to outpace East
844 Antarctic gains. *Earth and Planetary Science Letters*, *415*, 134-141. doi:10.1016/j.epsl.2015.01.029

845 Hayes, D. E., Frakes, L. A., Barrett, P. J., Burns, D. A., Chen, P.-H., Ford, A. B., Kaneps, A. G., Kemp, E. M.,
846 McCollum, D. W., Piper, D. J. W., Wall, R. E., & Webb, P. N. (1973). *Sites 270, 271, 272*. Retrieved from
847 Texas A & M University, Ocean Drilling Program, College Station, TX, United States.

848 Hesse, R., Khodabakhsh, S., Klauke, I., & Ryan, W. B. F. (1997). Asymmetrical turbid surface-plume
849 deposition near ice-outlets of the Pleistocene Laurentide ice sheet in the Labrador Sea. *Geo-Marine*
850 *Letters*, *17*(3), 179-187. doi:10.1007/s003670050024

851 Hilgen, F. J., Lourens, L. J., Van Dam, J. A., Beu, A. G., Boyes, A. F., Cooper, R. A., Krijgsman, W., Ogg, J. G.,
852 Piller, W. E., & Wilson, D. S. (2012). Chapter 29 - The Neogene Period. In F. M. Gradstein, J. G. Ogg, M. D.
853 Schmitz, & G. M. Ogg (Eds.), *The Geologic Time Scale* (pp. 923-978). Boston: Elsevier.

854 Hillenbrand, C. D., Ehrmann, W., Larter, R. D., Benetti, S., Dowdeswell, J. A., Ó Cofaigh, C., Graham, A. G.
855 C., & Grobe, H. (2009a). Clay mineral provenance of sediments in the southern Bellingshausen Sea reveals

856 drainage changes of the West Antarctic Ice Sheet during the Late Quaternary. *Marine Geology*, 265(1), 1-
857 18. doi:10.1016/j.margeo.2009.06.009

858 Hillenbrand, C. D., Kuhn, G., & Frederichs, T. (2009b). Record of a Mid-Pleistocene depositional anomaly
859 in West Antarctic continental margin sediments: an indicator for ice-sheet collapse? *Quaternary Science*
860 *Reviews*, 28(13), 1147-1159. doi:10.1016/j.quascirev.2008.12.010

861 Hughes, T. (1973). Is the west Antarctic Ice Sheet disintegrating? *Journal of Geophysical Research (1896-*
862 *1977)*, 78(33), 7884-7910. doi:10.1029/JC078i033p07884

863 Jacobs, S. S. (1991). On the nature and significance of the Antarctic Slope Front. *Marine Chemistry*, 35(1-
864 4), 9-24. doi:10.1016/s0304-4203(09)90005-6

865 Jacobs, S. S., Amos, A. F., & Bruchhausen, P. M. (1970). Ross sea oceanography and antarctic bottom
866 water formation. *Deep Sea Research and Oceanographic Abstracts*, 17(6), 935-962. doi:10.1016/0011-
867 7471(70)90046-X

868 Jacobs, S. S., & Haines, W. E. (1982). Oceanographic data in the Ross Sea and along George V Coast 1976-
869 1979.

870 Kennett, J. P. (1968). The fauna of the Ross Sea. Part 6: Ecology and distribution of Foraminifera. *New*
871 *Zealand Department of Scientific and Industrial Research Bulletin*, 186.

872 Keys, H., & Fowler, D. (1989). Sources and Movement of Icebergs in the South-West Ross Sea, Antarctica.
873 *Annals of Glaciology*, 12, 85-88. doi:10.3189/S026030550000700X

874 Kim, S., De Santis, L., Hong, J. K., Cottlerle, D., Petronio, L., Colizza, E., Kim, Y. G., Kang, S. G., Kim, H. J.,
875 Kim, S., Wardell, N., Geletti, R., Bergamasco, A., McKay, R., Jin, Y. K., & Kang, S. H. (2018). Seismic
876 stratigraphy of the Central Basin in northwestern Ross Sea slope and rise, Antarctica: Clues to the late
877 Cenozoic ice-sheet dynamics and bottom current activity. *Marine Geology*, 395, 363-379.
878 doi:10.1016/j.margeo.2017.10.013

879 King, E. L., Hafliðason, H., Sejrup, H. P., & Løvlie, R. (1998). Glacigenic debris flows on the North Sea
880 Trough Mouth Fan during ice stream maxima. *Marine Geology*, 152(1), 217-246. doi:10.1016/S0025-
881 3227(98)00072-3

882 Kurtz, D. D., & Anderson, J. B. (1979). Recognition and sedimentologic description of recent debris flow
883 deposits from the Ross and Weddell Seas, Antarctica. *Journal of Sedimentary Research*, 49(4), 1159-1169.
884 doi:10.1306/212F78D8-2B24-11D7-8648000102C1865D

885 Kuvaas, B., Kristoffersen, Y., Guseva, J., Leitchenkov, G., Gandjukhin, V., Løvås, O., Sand, M., & Brekke, H.
886 (2005). Interplay of turbidite and contourite deposition along the Cosmonaut Sea/Enderby Land margin,
887 East Antarctica. *Marine Geology*, 217(1), 143-159. doi:[10.1016/j.margeo.2005.02.025](https://doi.org/10.1016/j.margeo.2005.02.025)

888 Kuvaas, B., & Leitchenkov, G. (1992). Glaciomarine turbidite and current controlled deposits in Prydz Bay,
889 Antarctica. *Marine Geology*, 108(3), 365-381. doi:[10.1016/0025-3227\(92\)90205-V](https://doi.org/10.1016/0025-3227(92)90205-V)

890 Laberg, J. S., & Vorren, T. O. (1995). Late Weichselian submarine debris flow deposits on the Bear Island
891 Trough Mouth Fan. *Marine Geology*, 127(1), 45-72. doi:[10.1016/0025-3227\(95\)00055-4](https://doi.org/10.1016/0025-3227(95)00055-4)

892 Laberg, J. S., & Vorren, T. O. (1996). The Middle and Late Pleistocene evolution and the Bear Island
893 Trough Mouth Fan. *Global and Planetary Change*, 12(1), 309-330. doi:10.1016/0921-8181(95)00026-7

894 Laberg, J. S., & Vorren, T. O. (2000). Flow behaviour of the submarine glacigenic debris flows on the Bear
895 Island Trough Mouth Fan, western Barents Sea. *Sedimentology*, 47(6), 1105-1117. doi: 10.1046/j.1365-
896 3091.2000.00343.x

897 Lee, J. I., McKay, R. M., Gollidge, N. R., Yoon, H. I., Yoo, K.-C., Kim, H. J., & Hong, J. K. (2017). Widespread
898 persistence of expanded East Antarctic glaciers in the southwest Ross Sea during the last deglaciation.
899 *Geology*, 45(5), 403-406. doi:10.1130/g38715.1

900 Licht, K. J., Dunbar, N. W., Andrews, J. T., & Jennings, A. E. (1999). Distinguishing subglacial till and glacial
901 marine diamictos in the western Ross Sea, Antarctica: Implications for a last glacial maximum grounding
902 line. *GSA Bulletin*, 111(1), 91-103. doi:10.1130/0016-7606(1999)111<0091:Dstagm>2.3.Co;2

903 Lindeque, A., Gohl, K., Henrys, S., Wobbe, F., & Davy, B. (2016). Seismic stratigraphy along the Amundsen
904 Sea to Ross Sea continental rise: A cross-regional record of pre-glacial to glacial processes of the West
905 Antarctic margin. *Palaeogeography, Palaeoclimatology, Palaeoecology*, *443*, 183-202.
906 doi:10.1016/j.palaeo.2015.11.017

907 Lisiecki, L. E., & Raymo, M. E. (2005). A Pliocene-Pleistocene stack of 57 globally distributed benthic $\delta^{18}\text{O}$
908 records. *Paleoceanography*, *20*(1). doi: 10.1029/2004PA001071

909 Lourens, L., Hilgen, F., Shackleton, N.J., Laskar, J., and Wilson, D. (2004). The Neogene period. In F. M.
910 Gradstein, Ogg, J.G., and Smith, A. (Ed.), *A Geologic Time Scale (2004)* (pp. 409–440). Cambridge, United
911 Kingdom: Cambridge University Press.

912 Lowe, D. R. (1982). Sediment gravity flows; II, Depositional models with special reference to the deposits
913 of high-density turbidity currents. *Journal of Sedimentary Research*, *52*(1), 279-297.
914 doi:10.1306/212F7F31-2B24-11D7-8648000102C1865D

915 Lucchi, R. G., Camerlenghi, A., Rebesco, M., Colmenero-Hidalgo, E., Sierro, F. J., Sagnotti, L., Urgeles, R.,
916 Melis, R., Morigi, C., Bárcena, M. A., Giorgetti, G., Villa, G., Persico, D., Flores, J. A., Rigual-Hernández, A.
917 S., Pedrosa, M. T., Macri, P., & Caburlotto, A. (2013). Postglacial sedimentary processes on the
918 Storfjorden and Kveithola trough mouth fans: Significance of extreme glacial marine sedimentation. *Global
919 and Planetary Change*, *111*, 309-326. doi:10.1016/j.gloplacha.2013.10.008

920 Lucchi, R. G., & Rebesco, M. (2007). Glacial contourites on the Antarctic Peninsula margin: insight for
921 palaeoenvironmental and palaeoclimatic conditions. *Geological Society, London, Special Publications*,
922 *276*(1), 111-127. doi:10.1144/GSL.SP.2007.276.01.06

923 Lucchi, R. G., Rebesco, M., Camerlenghi, A., Busetti, M., Tomadin, L., Villa, G., Persico, D., Morigi, C.,
924 Bonci, M. C., & Giorgetti, G. (2002). Mid-late Pleistocene glacial marine sedimentary processes of a high-
925 latitude, deep-sea sediment drift (Antarctic Peninsula Pacific margin). *Marine Geology*, *189*(3-4), 343-370.
926 doi:10.1016/S0025-3227(02)00470-X

927 Majewski, W., Bart, P. J., & McGlannan, A. J. (2018). Foraminiferal assemblages from ice-proximal paleo-
928 settings in the Whales Deep Basin, eastern Ross Sea, Antarctica. *Palaeogeography, Palaeoclimatology,*
929 *Palaeoecology*, 493, 64-81. doi:10.1016/j.palaeo.2017.12.041

930 McKay, R., Bendle, J., Cook, C., Dunbar, G., Dunbar, R. B., Escutia, C., González, J. J., Jiménez, F., Naish, T.,
931 Passchier, S., Riesselman, C. R., Scherer, R. P., Tauxe, L., Toney, J. L., van de Flierdt, T., Welsh, K. J., &
932 Scientists, I. E. S. (2011). *Early to Mid-Pleistocene Warm Events at the Antarctic Margin*.
933 <https://ui.adsabs.harvard.edu/abs/2011AGUFMPP44A..08M>

934 McKay, R. M., Browne, G., Carter, L., Cowan, E. A., Dunbar, G., Krissek, L., Naish, T., Powell, R. D., Reed, J.,
935 Talarico, F. M., & Wilch, T. (2009). The stratigraphic signature of the late Cenozoic Antarctic Ice Sheets in
936 the Ross Embayment. *Geological Society of America Bulletin*, 121(11-12), 1537-1561.
937 doi:10.1130/b26540.1

938 McKay, R. M., De Santis, L., Kulhanek, D. K., Ash, J. L., Beny, F., Browne, I. M., Cortese, G., Cordeiro de
939 Sousa, I. M., Dodd, J. P., Esper, O. M., Gales, J. A., Harwood, D. M., Ishino, S., Keisling, B. A., Kim, S., Kim,
940 S., Laberg, J. S., Leckie, R. M., Müller, J., Patterson, M. O., Romans, B. W., Romero, O. E., Sangiorgi, F.,
941 Seki, O., Shevenell, A. E., Singh, S. M., Sugisaki, S. T., van de Flierdt, T., van Peer, T. E., Xiao, W., and Xiong,
942 Z., and the Expedition 374 Scientists. (2019a). Expedition 374 methods. *Proceedings of the International*
943 *Ocean Discovery Program, 374: College Station, TX (International Ocean Discovery Program)*.
944 doi:10.14379/iodp.proc.374.102.2019

945 McKay, R. M., De Santis, L., Kulhanek, D. K., Ash, J. L., Beny, F., Browne, I. M., Cortese, G., Cordeiro de
946 Sousa, I. M., Dodd, J. P., Esper, O. M., Gales, J. A., Harwood, D. M., Ishino, S., Keisling, B. A., Kim, S., Kim,
947 S., Laberg, J. S., Leckie, R. M., Müller, J., Patterson, M. O., Romans, B. W., Romero, O. E., Sangiorgi, F.,
948 Seki, O., Shevenell, A. E., Singh, S. M., Sugisaki, S. T., van de Flierdt, T., van Peer, T. E., Xiao, W., and Xiong,
949 Z., and the Expedition 374 Scientists. (2019b). Site U1525. *Proceedings of the International Ocean*
950 *Discovery Program, 374: College Station, TX (International Ocean Discovery Program)*.
951 doi:10.14379/iodp.proc.374.107.2019

952 McKay, R. M., Naish, T., Powell, R. D., Barrett, P., Scherer, R. P., Talarico, F. M., Kyle, P., Monien, D., Kuhn,
953 G., Jackolski, C., & Williams, T. (2012). Pleistocene variability of Antarctic Ice Sheet extent in the Ross
954 Embayment. *Quaternary Science Reviews*, 34, 93-112. doi:10.1016/j.quascirev.2011.12.012

955 McMillan, M., Shepherd, A., Sundal, A., Briggs, K., Muir, A., Ridout, A., Hogg, A., & Wingham, D. (2014).
956 Increased ice losses from Antarctica detected by CryoSat-2. *Geophysical Research Letters*, 41(11), 3899-
957 3905. doi: h10.1002/2014GL060111

958 Melles, M. (1991). *Paläoglazologie und Paläozeanographie im Spätquartär am Kontinentalrand des*
959 *südlichen Weddellmeeres, Antarktis*. University of Bremen.

960 Michels, K. H., Rogenhagen, J., & Kuhn, G. (2001). Recognition of contour-current influence in mixed
961 contourite-turbidite sequences of the western Weddell Sea, Antarctica. *Marine Geophysical Researches*,
962 22(5-6), 465-485. doi:[10.1023/A:1016303817273](https://doi.org/10.1023/A:1016303817273)

963 Miramontes, E., Eggenhuisen, J. T., Jacinto, R. S., Poneti, G., Pohl, F., Normandeau, A., Campbell, D. C., &
964 Hernández-Molina, F. J. (2020). Channel-levee evolution in combined contour current–turbidity current
965 flows from flume-tank experiments. *Geology*, 48(4), 353-357. doi:10.1130/g47111.1

966 Morrison, A. K., Hogg, A. M., England, M. H., & Spence, P. (2020). Warm Circumpolar Deep Water
967 transport toward Antarctica driven by local dense water export in canyons. *Science Advances*, 6(18),
968 eaav2516. doi:10.1126/sciadv.aav2516

969 Mosola, A. B., & Anderson, J. B. (2006). Expansion and rapid retreat of the West Antarctic Ice Sheet in
970 eastern Ross Sea: possible consequence of over-extended ice streams? *Quaternary Science Reviews*,
971 25(17-18), 2177-2196. doi:10.1016/j.quascirev.2005.12.013

972 Mulder, T., Berry, J. A., & Piper, D. J. W. (1997). Links Between Morphology and Geotechnical
973 Characteristics of Large Debris Flow Deposits in the Albatross Area on the Scotian Slope (SE Canada).
974 *Marine Georesources & Geotechnology*, 15(3), 253-281. doi:10.1080/10641199709379947

975 Mulder, T., Faugères, J. C., & Gonthier, E. (2008). Chapter 21 Mixed Turbidite–Contourite Systems. In M.
976 Rebesco & A. Camerlenghi (Eds.), *Developments in Sedimentology* (Vol. 60, pp. 435-456): Elsevier.

977 Naish, T., Powell, R., Levy, R., Wilson, G., Scherer, R., Talarico, F., Krissek, L., Niessen, F., Pompilio, M., &
978 Wilson, T. (2009). Obliquity-paced Pliocene West Antarctic ice sheet oscillations. *Nature*, *458*(7236), 322.

979 Noormets, R., Dowdeswell, J. A., Larter, R. D., Ó Cofaigh, C., & Evans, J. (2009). Morphology of the upper
980 continental slope in the Bellingshausen and Amundsen Seas – Implications for sedimentary processes at
981 the shelf edge of West Antarctica. *Marine Geology*, *258*(1), 100-114. doi:10.1016/j.margeo.2008.11.011

982 Ó Cofaigh, C., Taylor, J., Dowdeswell, J. A., & Pudsey, C. J. (2003). Palaeo-ice streams, trough mouth fans
983 and high-latitude continental slope sedimentation. *Boreas*, *32*(1), 37-55.
984 doi:10.1080/03009480310001858

985 Orsi, A. H., & Wiederwohl, C. L. (2009). A recount of Ross Sea waters. *Deep Sea Research Part II: Topical*
986 *Studies in Oceanography*, *56*(13-14), 778-795. doi:10.1016/j.dsr2.2008.10.033

987 Passchier, S., Browne, G., Field, B., Fielding, C. R., Krissek, L. A., Panter, K., Pekar, S. F., & Team, a. A.-S. S.
988 (2011). Early and middle Miocene Antarctic glacial history from the sedimentary facies distribution in the
989 AND-2A drill hole, Ross Sea, Antarctica. *GSA Bulletin*, *123*(11-12), 2352-2365. doi:10.1130/b30334.1

990 Passchier, S., O'Brien, P. E., Damuth, J. E., Januszczak, N., Handwerger, D. A., & Whitehead, J. M. (2003).
991 Pliocene–Pleistocene glaciomarine sedimentation in eastern Prydz Bay and development of the Prydz
992 trough-mouth fan, ODP Sites 1166 and 1167, East Antarctica. *Marine Geology*, *199*(3), 279-305.
993 doi:10.1016/S0025-3227(03)00160-9

994 Patterson, M. O., McKay, R., Naish, T., Escutia, C., Jimenez-Espejo, F. J., Raymo, M. E., Meyers, S. R.,
995 Tauxe, L., Brinkhuis, H., Klaus, A., Fehr, A., Bendle, J. A. P., Bijl, P. K., Bohaty, S. M., Carr, S. A., Dunbar, R.
996 B., Flores, J. A., Gonzalez, J. J., Hayden, T. G., Iwai, M., Katsuki, K., Kong, G. S., Nakai, M., Olney, M. P.,
997 Passchier, S., Pekar, S. F., Pross, J., Riesselman, C. R., Röhl, U., Sakai, T., Shrivastava, P. K., Stickley, C. E.,
998 Sugasaki, S., Tuo, S., van de Flierdt, T., Welsh, K., Williams, T., Yamane, M., & Scientists, I. E. (2014).

999 Orbital forcing of the East Antarctic ice sheet during the Pliocene and Early Pleistocene. *Nature*
1000 *geoscience*, 7(11), 841-847. doi:10.1038/ngeo2273

1001 Peakall, J., McCaffrey, B., & Kneller, B. (2000). A Process Model for the Evolution, Morphology, and
1002 Architecture of Sinuous Submarine Channels. *Journal of Sedimentary Research - J SEDIMENT RES*, 70, 434-
1003 448. doi:10.1306/2DC4091C-0E47-11D7-8643000102C1865D

1004 Perotti, M., Andreucci, B., Talarico, F., Zattin, M., & Langone, A. (2017). Multianalytical provenance
1005 analysis of Eastern Ross Sea LGM till sediments (Antarctica): Petrography, geochronology, and
1006 thermochronology detrital data. *Geochemistry, Geophysics, Geosystems*, 18(6), 2275-2304.
1007 doi:[10.1002/2016GC006728](https://doi.org/10.1002/2016GC006728)

1008 Piper, D. J. W., & Brisco, C. D. (1975). Deep-Water Continental Margin Sedimentation, DSDP, Leg 28,
1009 Antarctica. *Initial Reports of the Deep Sea Drilling Project*, 28, 727-755.
1010 doi:10.2973/dsdp.proc.28.121.1975

1011 Piper, D. J. W., & Normark, W. R. (1983). Turbidite depositional patterns and flow characteristics, Navy
1012 Submarine Fan, California Borderland. *Sedimentology*, 30(5), 681-694. doi:[10.1111/j.1365-
1013 3091.1983.tb00702.x](https://doi.org/10.1111/j.1365-3091.1983.tb00702.x)

1014 Pollard, D., & DeConto, R. M. (2009). Modelling West Antarctic ice sheet growth and collapse through the
1015 past five million years. *Nature*, 458, 329. doi:10.1038/nature07809

1016 Prothro, L. O., Simkins, L. M., Majewski, W., & Anderson, J. B. (2018). Glacial retreat patterns and
1017 processes determined from integrated sedimentology and geomorphology records. *Marine Geology*, 395,
1018 104-119. doi:10.1016/j.margeo.2017.09.012

1019 Pudsey, C. J. (2000). Sedimentation on the continental rise west of the Antarctic Peninsula over the last
1020 three glacial cycles. *Marine Geology*, 167(3), 313-338. doi:10.1016/S0025-3227(00)00039-6

1021 Pudsey, C. J. (2002). Neogene Record of Antarctic Peninsula Glaciation in Continental Rise Sediments:
1022 ODP Leg 178, Site 1095. *Proceedings of the Ocean Drilling Program: Scientific Results*, 178, 1-25.
1023 doi:10.2973/odp.proc.sr.178.214.2001

1024 Pudsey, C. J., & Camerlenghi, A. (1998). Glacial–interglacial deposition on a sediment drift on the Pacific
1025 margin of the Antarctic Peninsula. *Antarctic Science*, 10(3), 286-308. doi:10.1017/S0954102098000376

1026 Rebesco, M., Camerlenghi, A., Geletti, R., & Canals, M. (2006). Margin architecture reveals the transition
1027 to the modern Antarctic ice sheet ca. 3 Ma. *Geology*, 34(4), 301-304. doi:10.1130/g22000.1

1028 Rebesco, M., Camerlenghi, A., Volpi, V., Neagu, C., Accettella, D., Lindberg, B., Cova, A., & Zgur, F. (2007).
1029 Interaction of processes and importance of contourites: insights from the detailed morphology of
1030 sediment Drift 7, Antarctica. *Geological Society, London, Special Publications*, 276(1), 95-110.
1031 doi:10.1144/gsl.Sp.2007.276.01.05

1032 Rebesco, M., Hernandez-Molina, F. J., Van Rooij, D., & Wahlin, A. (2014). Contourites and associated
1033 sediments controlled by deep-water circulation processes: State-of-the-art and future considerations.
1034 *Marine Geology*, 352, 111-154. doi:10.1016/j.margeo.2014.03.011

1035 Rignot, E., Mouginot, J., Scheuchl, B., van den Broeke, M., van Wessem, M. J., & Morlighem, M. (2019).
1036 Four decades of Antarctic Ice Sheet mass balance from 1979–2017. *Proceedings of the National Academy
1037 of Sciences*, 116(4), 1095-1103. doi:10.1073/pnas.1812883116

1038 Salles, T., Marchès, E., Dyt, C., Griffiths, C., Hanquiez, V., & Mulder, T. (2010). Simulation of the
1039 interactions between gravity processes and contour currents on the Algarve Margin (South Portugal)
1040 using the stratigraphic forward model Sedsim. *Sedimentary Geology*, 229(3), 95-109.
1041 doi:[10.1016/j.sedgeo.2009.05.007](https://doi.org/10.1016/j.sedgeo.2009.05.007)

1042 Scherer, R. P., Bohaty, S. M., Dunbar, R. B., Esper, O., Flores, J.-A., Gersonde, R., Harwood, D. M., Roberts,
1043 A. P., & Taviani, M. (2008). Antarctic records of precession-paced insolation-driven warming during early
1044 Pleistocene Marine Isotope Stage 31. *Geophysical Research Letters*, 35(3). doi:10.1029/2007gl032254

1045 Schröder, L., Horwath, M., Dietrich, R., Helm, V., van den Broeke, M. R., & Ligtenberg, S. R. M. (2019).
1046 Four decades of Antarctic surface elevation changes from multi-mission satellite altimetry. *The*
1047 *Cryosphere*, 13(2), 427-449. doi:10.5194/tc-13-427-2019

1048 Shanmugam, G. (1997). The Bouma Sequence and the turbidite mind set. *Earth-Science Reviews*, 42(4),
1049 201-229. doi:10.1016/S0012-8252(97)81858-2

1050 Shepherd, A., Ivins, E., Rignot, E., Smith, B., van den Broeke, M., Velicogna, I., Whitehouse, P., Briggs, K.,
1051 Joughin, I., & Krinner, G. (2018). Mass balance of the Antarctic Ice Sheet from 1992 to 2017. *Nature*, 556,
1052 219–222. doi:10.1038/s41586-018-0179-y

1053 Shipp, S., Anderson, J., & Domack, E. (1999). Late Pleistocene–Holocene retreat of the West Antarctic Ice-
1054 Sheet system in the Ross Sea: Part 1—Geophysical results. *GSA Bulletin*, 111(10), 1486-1516.
1055 doi:10.1130/0016-7606(1999)111<1486:Lphrot>2.3.Co;2

1056 Sinclair, H. D., & Tomasso, M. (2002). Depositional Evolution of Confined Turbidite Basins. *Journal of*
1057 *Sedimentary Research*, 72(4), 451-456. doi:10.1306/111501720451

1058 Smith, J. A., Graham, A. G. C., Post, A. L., Hillenbrand, C.-D., Bart, P. J., & Powell, R. D. (2019). The
1059 marine geological imprint of Antarctic ice shelves. *Nature Communications*, 10(1), 5635.
1060 doi:10.1038/s41467-019-13496-5

1061 Stein, K., Timmermann, A., Kwon, E. Y., & Friedrich, T. (2020). Timing and magnitude of Southern Ocean
1062 sea ice/carbon cycle feedbacks. *Proceedings of the National Academy of Sciences*, 117(9), 4498.
1063 doi:10.1073/pnas.1908670117

1064 Stow, D. A. V. (1985). Fine-grained sediments in deep water: An overview of processes and facies models.
1065 *Geo-Marine Letters*, 5(1), 17-23. doi:10.1007/BF02629792

1066 Stow, D. A. V., Faugères, J.-C., Howe, J. A., Pudsey, C. J., & Viana, A. R. (2002). Bottom currents,
1067 contourites and deep-sea sediment drifts: current state-of-the-art. *Geological Society, London, Memoirs*,
1068 22(1), 7. doi:10.1144/GSL.MEM.2002.022.01.02

1069 Stow, D. A. V., & Piper, D. J. W. (1984). Deep-water fine-grained sediments: facies models. *Geological*
1070 *Society, London, Special Publications*, 15(1), 611-646. doi:10.1144/gsl.Sp.1984.015.01.38

1071 Stow, D. A. V., & Smillie, Z. (2020). Distinguishing between Deep-Water Sediment Facies: Turbidites,
1072 Contourites and Hemipelagites. *Geosciences*, 10, 68. doi:10.3390/geosciences10020068

1073 Teitler, L., Florindo, F., Warnke, D. A., Filippelli, G. M., Kupp, G., & Taylor, B. (2015). Antarctic Ice Sheet
1074 response to a long warm interval across Marine Isotope Stage 31: A cross-latitudinal study of iceberg-
1075 rafted debris. *Earth and Planetary Science Letters*, 409, 109-119. doi:10.1016/j.epsl.2014.10.037

1076 Tripsanas, E. K., & Piper, D. J. W. (2008). Glaciogenic debris-flow deposits of Orphan Basin, offshore
1077 eastern Canada: sedimentological and rheological properties, origin, and relationship to meltwater
1078 discharge. *Journal of Sedimentary Research*, 78(11), 724-744. doi:10.2110/jsr.2008.082

1079 Tziperman, E., & Gildor, H. (2003). On the mid-Pleistocene transition to 100-kyr glacial cycles and the
1080 asymmetry between glaciation and deglaciation times. *Paleoceanography*, 18(1), 1-1-1-8.
1081 doi:10.1029/2001pa000627

1082 Villa, G., Lupi, C., Cobianchi, M., Florindo, F., & Pekar, S. F. (2008). A Pleistocene warming event at 1 Ma in
1083 Prydz Bay, East Antarctica: Evidence from ODP Site 1165. *Palaeogeography, Palaeoclimatology,*
1084 *Palaeoecology*, 260(1), 230-244. doi:10.1016/j.palaeo.2007.08.017

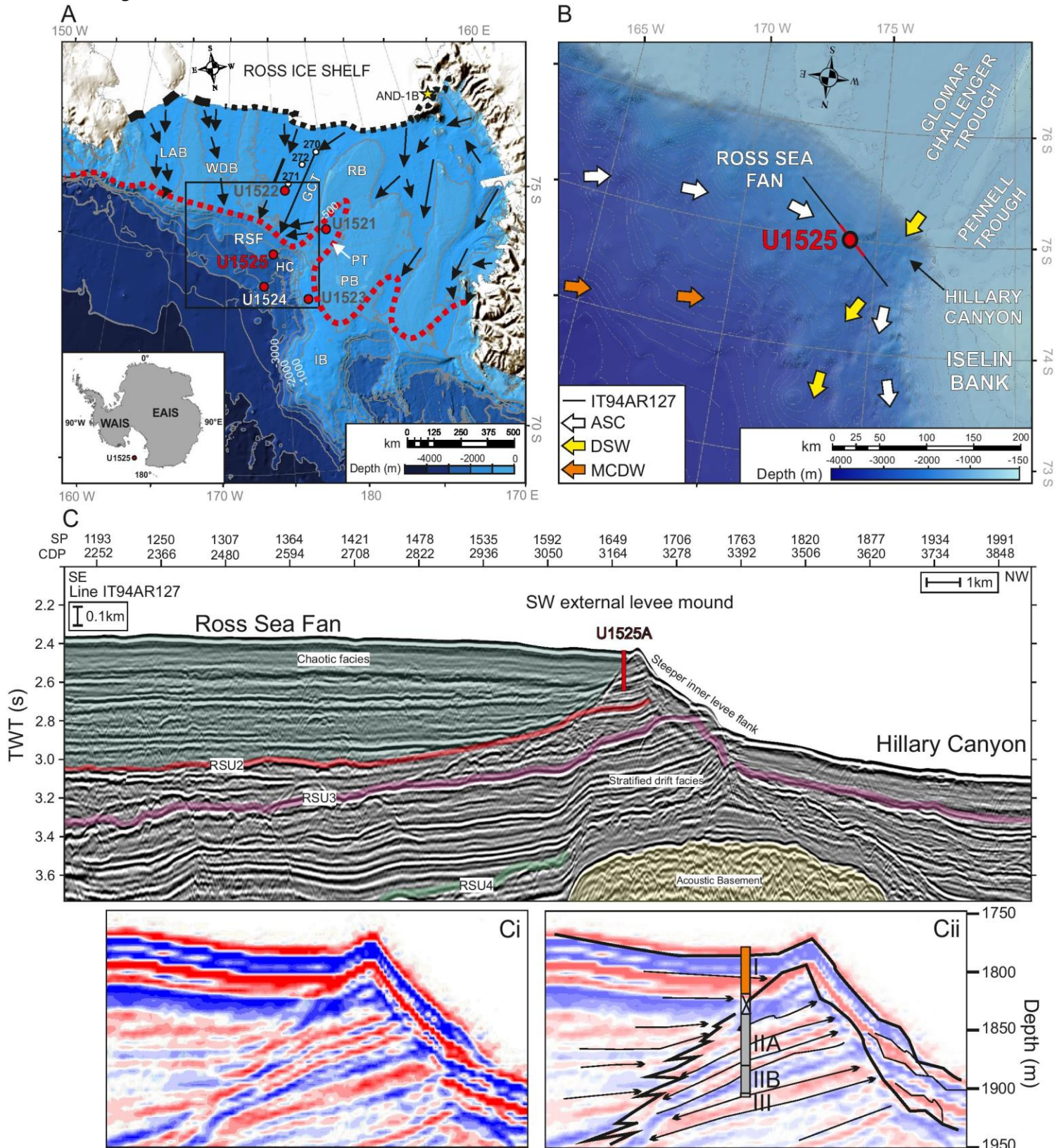
1085 Villa, G., Persico, D., Wise, S. W., & Gadaleta, A. (2012). Calcareous nannofossil evidence for Marine
1086 Isotope Stage 31 (1Ma) in Core AND-1B, ANDRILL McMurdo Ice Shelf Project (Antarctica). *Global and*
1087 *Planetary Change*, 96-97, 75-86. doi:10.1016/j.gloplacha.2009.12.003

1088 Vorren, T. O., & Laberg, J. S. (1997). Trough mouth fans — palaeoclimate and ice-sheet monitors.
1089 *Quaternary Science Reviews*, 16(8), 865-881. doi:10.1016/S0277-3791(97)00003-6

1090 Wang, D., & Hesse, R. (1996). Continental slope sedimentation adjacent to an ice-margin. II. Glaciomarine
1091 depositional facies on labrador slope and glacial cycles. *Marine Geology*, 135(1), 65-96.
1092 doi:10.1016/S0025-3227(96)00012-6

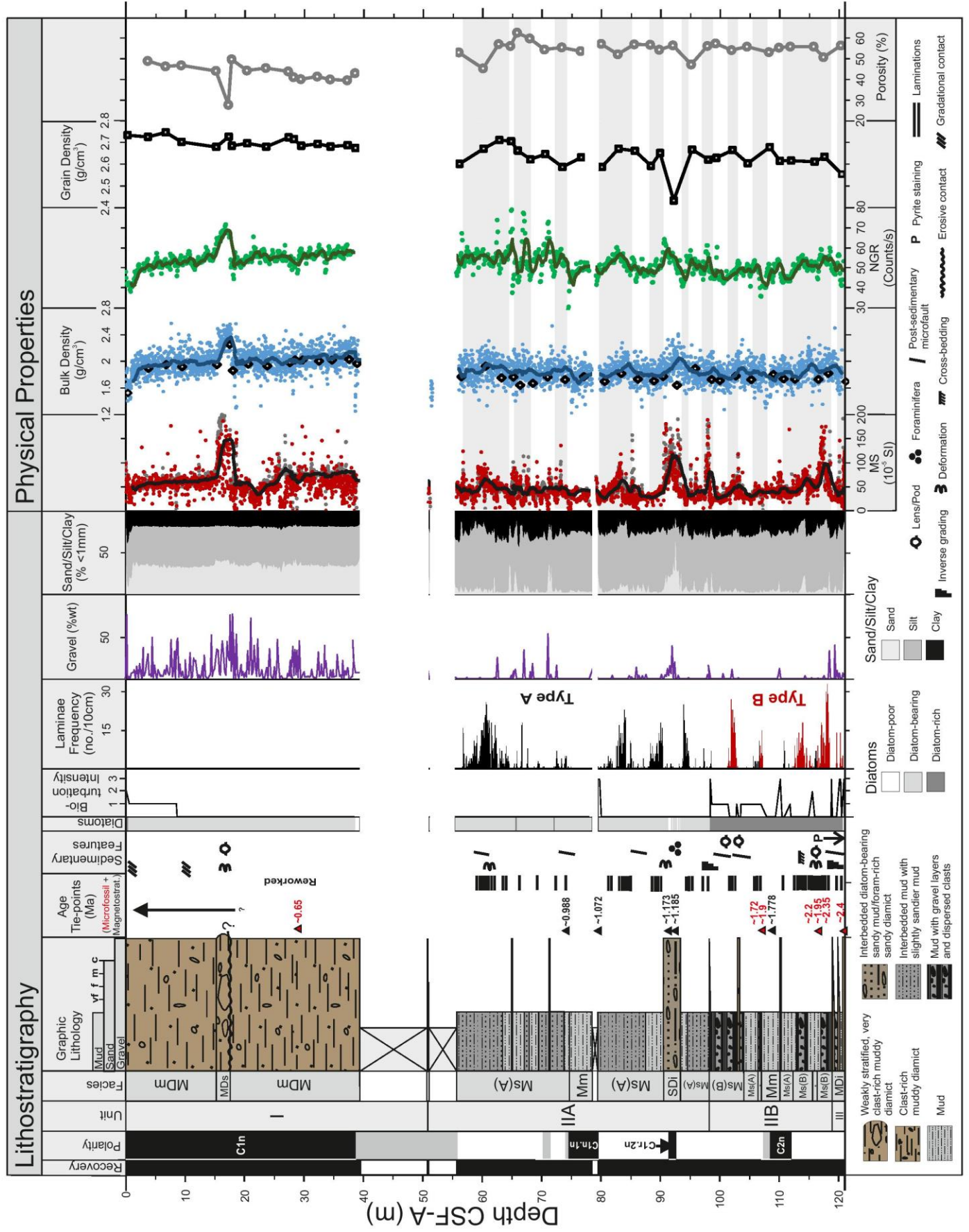
- 1093 Weertman, J. (1974). Stability of the Junction of an Ice Sheet and an Ice Shelf. *Journal of Glaciology*,
1094 13(67), 3-11. doi:10.3189 / S0022143000023327
- 1095 Wei, J. H., Finkelstein, D. B., Brigham-Grette, J., Castañeda, I. S., & Nowaczyk, N. (2014). Sediment colour
1096 reflectance spectroscopy as a proxy for wet/dry cycles at Lake El'gygytgyn, Far East Russia, during Marine
1097 Isotope Stages 8 to 12. *Sedimentology*, 61(6), 1793-1811. doi:10.1111/sed.12116
- 1098 Whitworth, T., & Orsi, A. H. (2006). Antarctic Bottom Water production and export by tides in the Ross
1099 Sea. *Geophysical Research Letters*, 33(12). doi:10.1029/2006GL026357
- 1100 Yu, B., Ma, Y., & Qi, X. (2013). Experimental Study on the Influence of Clay Minerals on the Yield Stress of
1101 Debris Flows. *Journal of Hydraulic Engineering*, 139(4), 364-373. doi:10.1061/(ASCE)HY.1943-
1102 7900.0000679
- 1103

1104 **Figures**

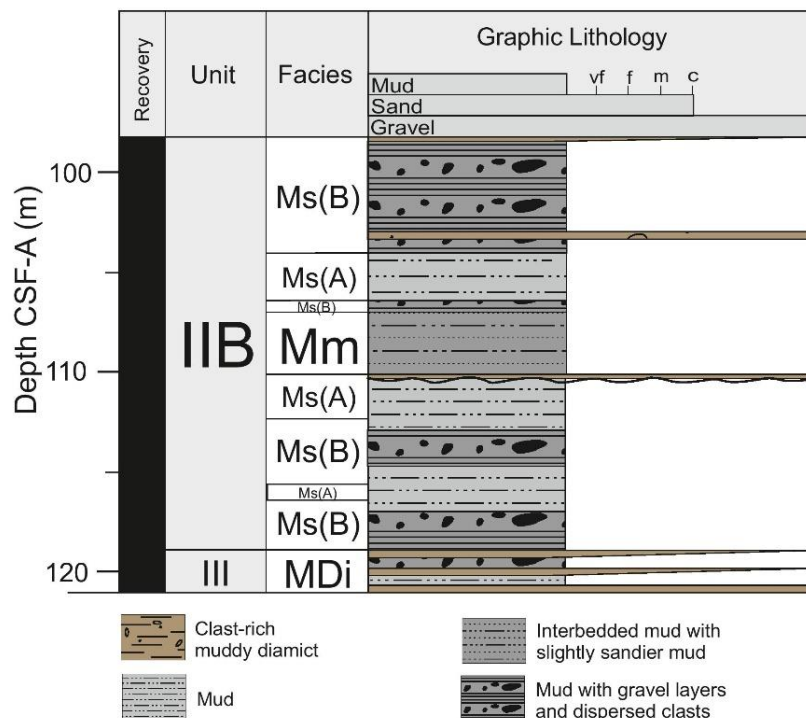


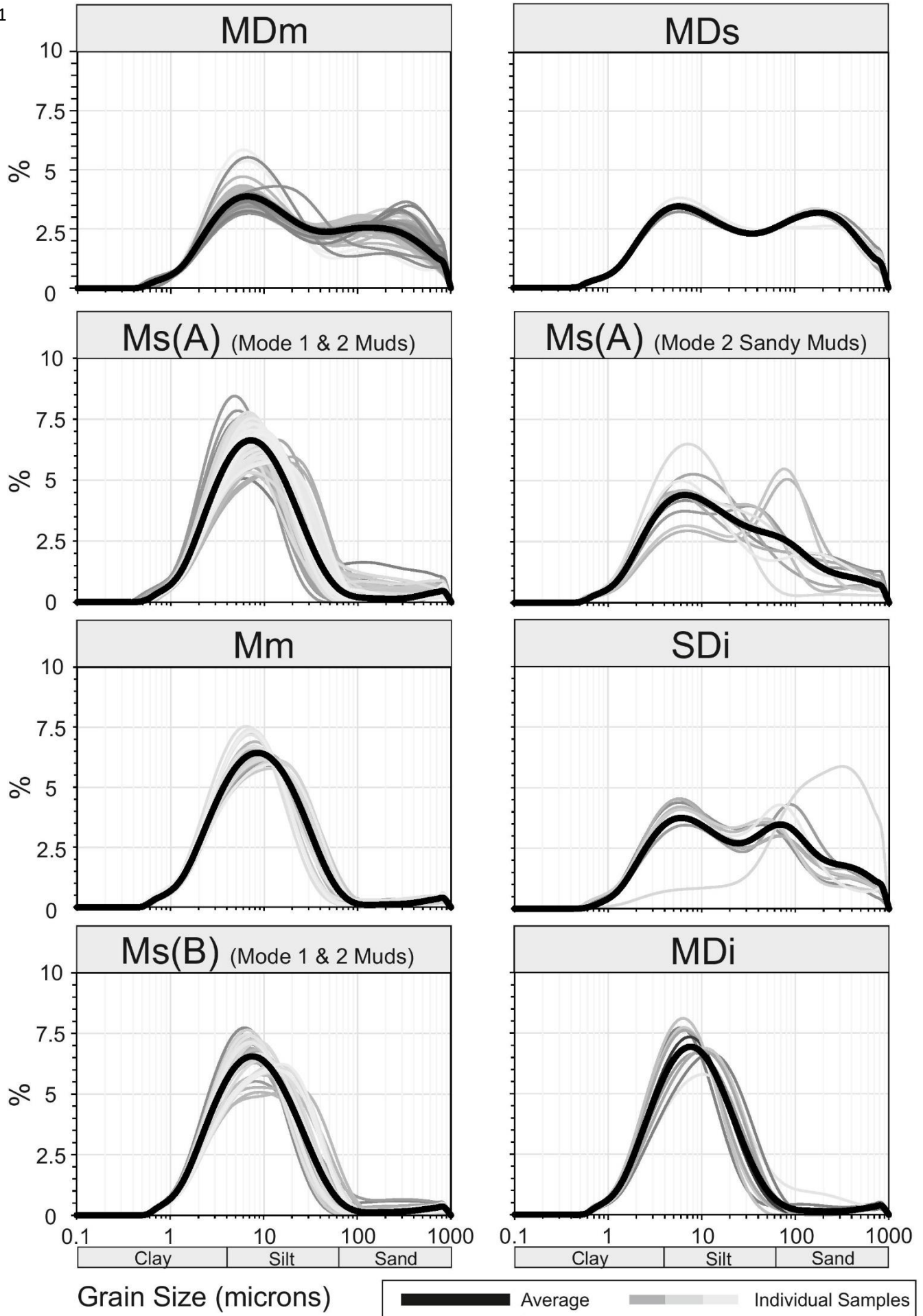
1105 **Figure 1:** Bathymetric maps of the Ross Sea, Antarctica. Map A shows the locations of Expedition 374 drill
 1106 sites (red circles), current ice front location (black dashed line), palaeo-grounding line during the last
 1107 glacial maximum (LGM; red dashed line) and palaeo-ice flow direction (black arrows) (adapted from

1108 Halberstadt et al., 2016 and Lee et al., 2017). GCT = Glomar Challenger Trough; HC = Hillary Canyon; IB =
1109 Iselin Bank; PB = Pennell Bank; PT = Pennell Trough; RB = Ross Bank; RSF = Ross Sea Fan. White circles
1110 270-272 represent sediment cores DSDP-270-272 from Deep Sea Drilling Program Leg 28 (Hayes et al.,
1111 1973). Yellow star is Antarctic Drilling Project (ANDRILL) sediment core AND-1B (Naish et al., 2009). Inset
1112 map shows location of Site U1525 in relation to Antarctica: EAIS = East Antarctic Ice Sheet and WAIS =
1113 West Antarctic Ice Sheet. The location of Map B is shown in the black box. Map B shows a more detailed
1114 view of Site U1525 as outlined in the dashed box in Map A where ASC = Antarctic Slope Current; DSW =
1115 Dense Shelf Water and MCDW = Modified Circumpolar Deep Water (Budillon et al., 2011; Orsi &
1116 Wiederwohl, 2009). Bathymetric data is sourced from the International Bathymetric Chart of the
1117 Southern Ocean spaced at A) 500m and B) 100m intervals (IBCSO; Arndt et al., 2013). Multichannel
1118 seismic line IT94AR-127 is shown in C (Finetti et al., unpubl. Data; available from the Antarctic Seismic
1119 Data Library System). Collected using 2x20 air gun (71.96 L) and 1500m streamer at a 50m shot interval.
1120 Adapted from McKay et al., 2019b. Highlighted green unit shows TMF facies above RSU2. Yellow unit
1121 shows location of acoustic basement. SP = Shot Point; CDP = Common Depth Point; TWT = Two-way
1122 travel time. Box Ci shows a zoomed-in, depth converted profile of line IT94AR-127 from where Hole
1123 U1525A was extracted. Box Cii shows the same profile with black lines and arrows showing our
1124 interpretation. The location of Hole U1525A and its principal lithostratigraphic units are also shown. Unit I
1125 is highlighted in red to show the boundary between the Ross Sea Fan deposits and the external levee
1126 mound deposits below (Units II and III). The section filled with a cross below Unit I represents an interval
1127 of no core recovery.

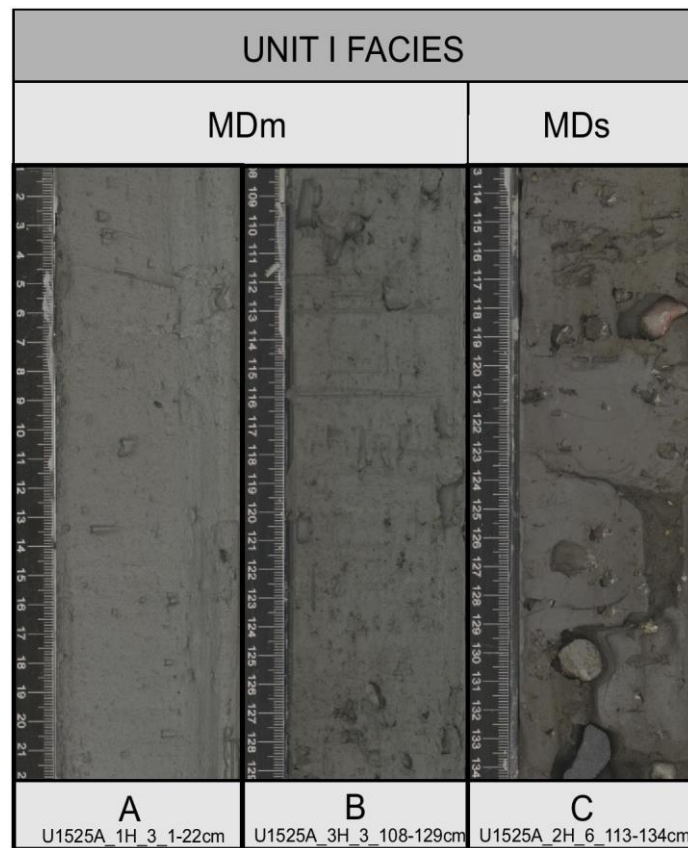


1129 **Figure 2.** Detailed lithostratigraphic interpretation of Hole U1525A (0-121.05 mbsf CSF-A), modified
 1130 from McKay et al., 2019b. Purple line is gravel %wt of whole sediment sample. Sand/silt/clay is %wt
 1131 <1mm fraction. Frequency of Type A and Type B laminae are shown in black and red respectively.
 1132 Physical properties data includes: section half multi-sensor core logger (SHMSL; red circles) and
 1133 whole round multi-sensor core logger (WRMSL) magnetic susceptibility (grey circles), black trend line
 1134 = WRMSL 50-point running mean; GRA (light blue circles) and discrete wet bulk density (grey-filled
 1135 diamonds), blue trend line = GRA 50-point running mean; green trend line = NGR 10-point running
 1136 mean from McKay et al., 2019b. Core recovery, polarity, age tie-points, sedimentary features,
 1137 diatom abundance and bioturbation intensity also from McKay et al., 2019b. See McKay et al., 2019b
 1138 for full magnetostratigraphy. Light grey bars highlight intervals of lamination to aid comparison.
 1139 **Figure 3:** Expanded view of facies in Subunit IIB/ Unit III.





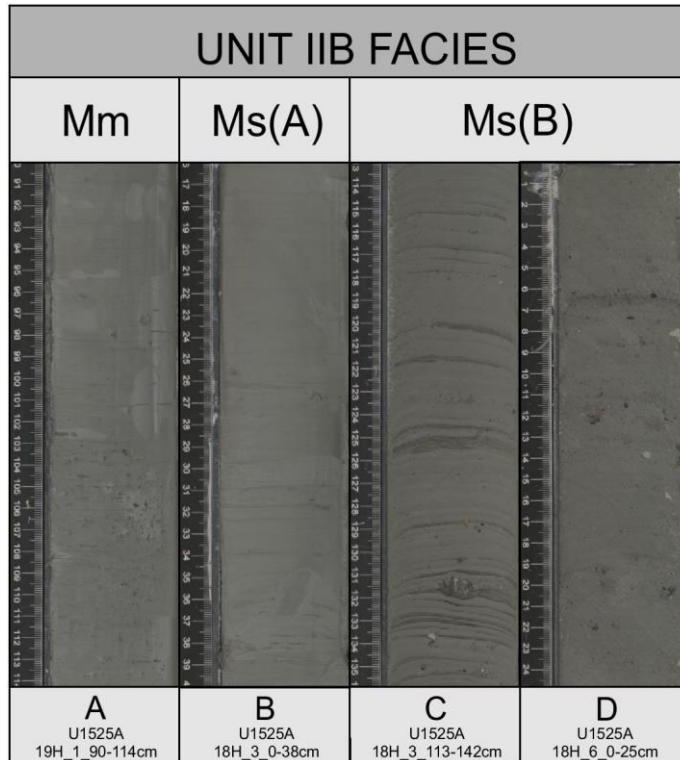
1141 **Figure 4:** Matrix grain size distributions for facies identified in U1525A: Massive Muddy Diamict,
 1142 MDm; Stratified Muddy Diamict, MDs; Mud with Type A Silt Laminae and Dispersed Clasts, Ms(A);
 1143 Massive Mud, Mm; Interbedded Diatom-bearing Muddy Diamict/Sandy Mud and Foraminifera-rich,
 1144 Clast-rich Sandy Diamict, SDi; Mud with Type B Silt and Gravel Laminae and Dispersed Clasts, Ms(B);
 1145 and Interbedded Mud and Muddy Diamict, MDi. Distributions for laminated facies Ms(A) and Ms(B)
 1146 do not include samples taken from laminae, only the matrix distribution. See supplementary
 1147 information for more description on Modes 1&2 for facies Ms(A) and Ms(B).



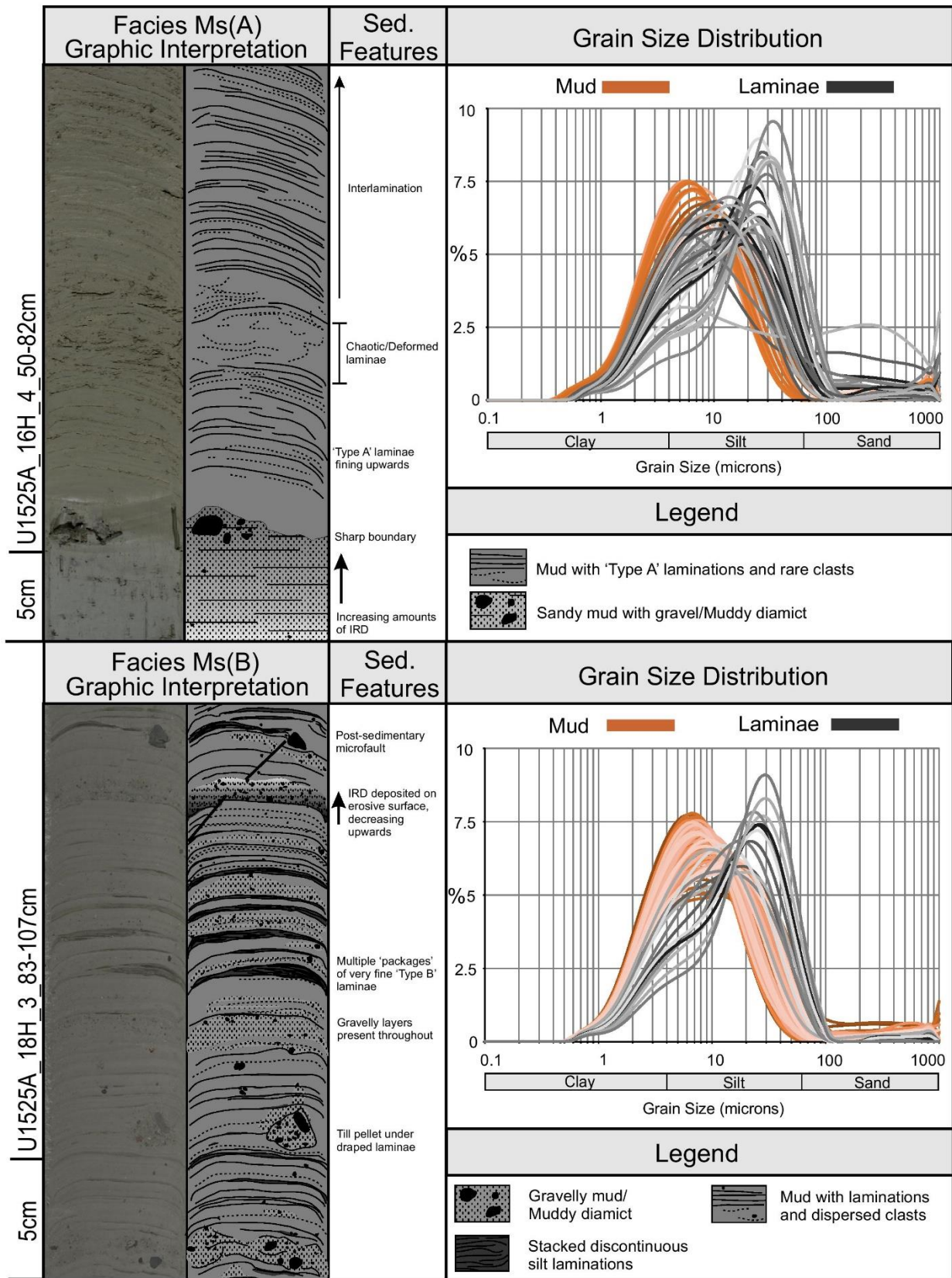
1148 **Figure 5:** Core images displaying facies in Unit I from: A) 3.01-3.22 mbsf; B) 22.19-22.4 mbsf and; C)
 1149 17.26-17.47 mbsf. Massive Muddy Diamict, MDm (A,B), displays varying amounts of clast content as
 1150 demonstrated in A and B. C displays facies MDs.



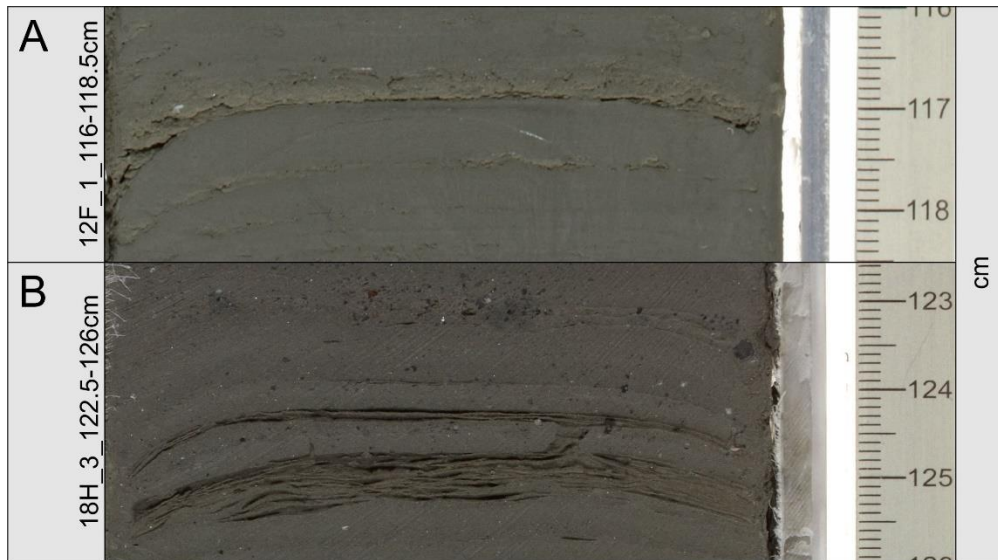
1151 **Figure 6:** Core images displaying facies in Subunit IIA from: A) 83.81-84.19 mbsf; B) 85.5-85.88 mbsf;
 1152 C) 76.11-76.49 mbsf; D) 92.12-92.5 mbsf. Mode 1 and 2 of facies Ms(A) are shown in A) strongly
 1153 Type A-interlaminated mud with silt laminae, and B) weakly Type A-laminated mud interbedded with
 1154 cm-scale sandy muds or diamicts (see Table 1 for in-depth facies description). Images C and D show
 1155 facies Mm and SDi, respectively.



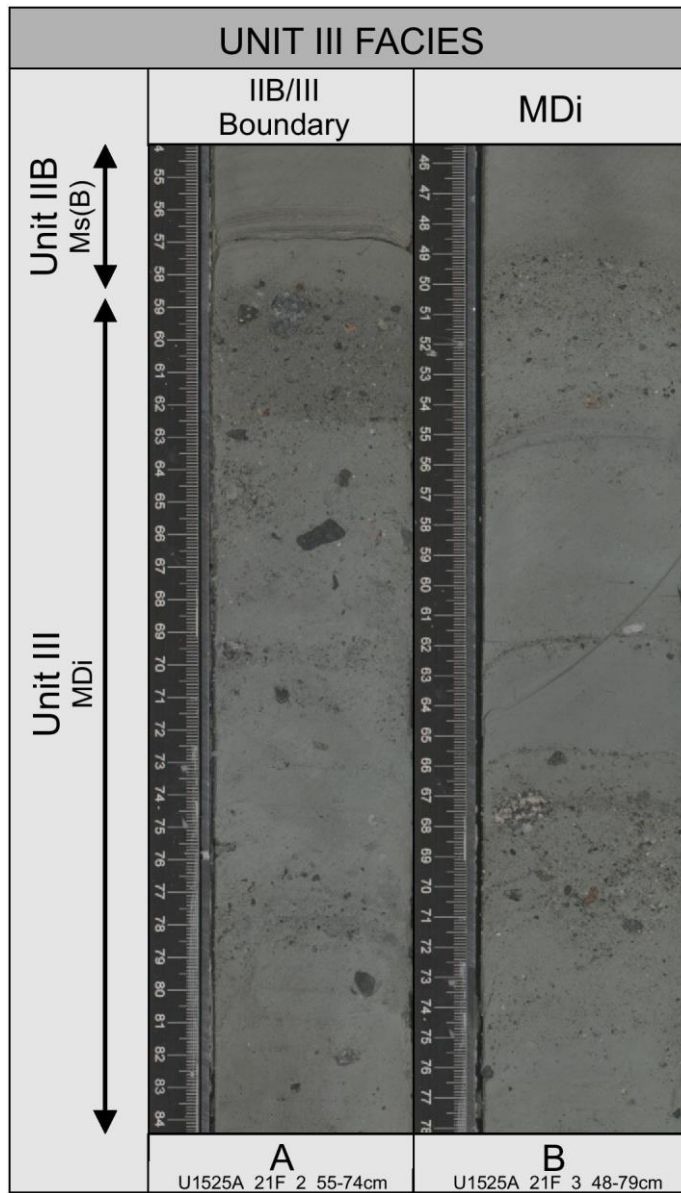
1156 **Figure 7:** Core images displaying facies in Subunit IIB from: A) 108.6-108.84 mbsf; B) 105.4-105.64
1157 mbsf; C) 102.32-102.55 mbsf; and D) 101.19-101.44 mbsf. Images A and B show facies Mm and
1158 Ms(A), respectively. Mode 1 and 2 of facies Ms(B) are shown in C) strongly Type B-interlaminated
1159 mud with silt laminae, and D) weakly Type B-laminated diatom-rich mud with dispersed clasts, gravel
1160 layers and cm-scale diamicts (see Table 1 for in-depth facies description).



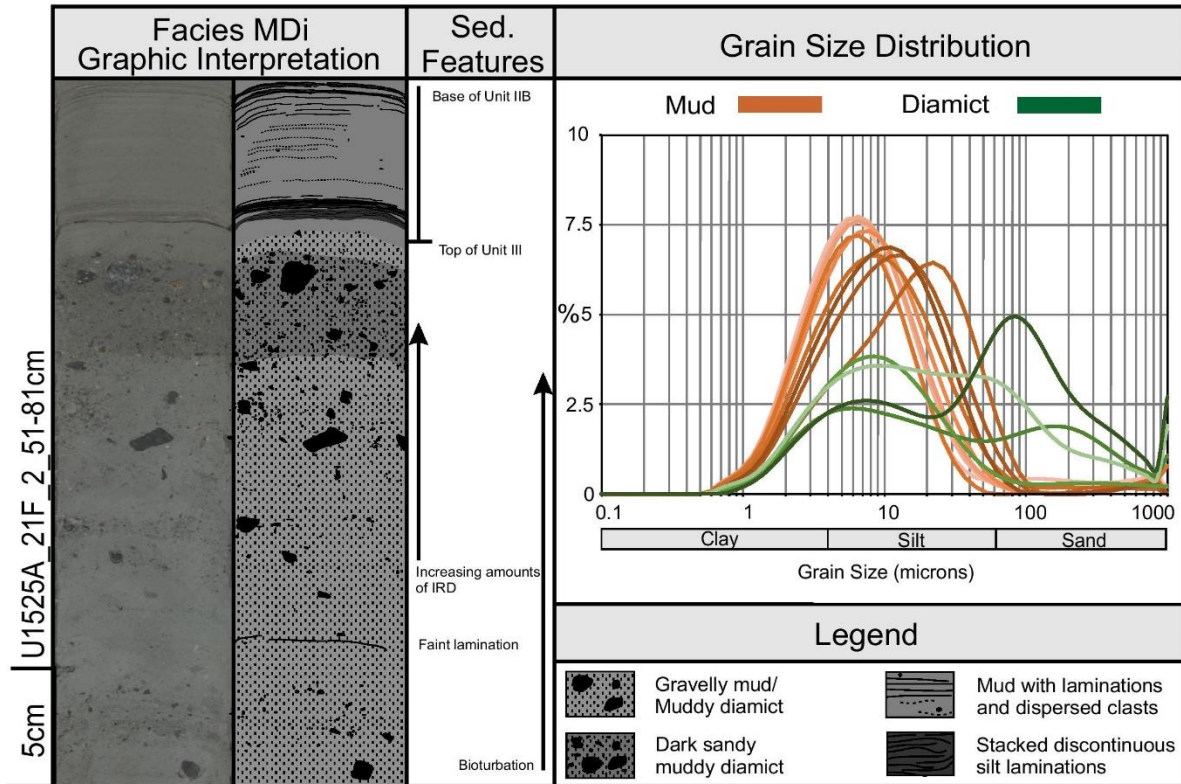
1162 **Figure 8:** Characteristics of laminated intervals in Unit II including interpreted illustration of
1163 sedimentary features and texture from Mud with Type A Silt Laminae and Dispersed Clasts facies,
1164 Ms(A) (83.96-84.29 mbsf) and Laminated Mud with Type B Silt Laminae and Gravel Layers facies,
1165 Ms(B) (102.02m-102.26 mbsf). Grain size spectra for laminae (grey) and mud (orange) include all
1166 samples taken from facies Ms(A) and facies Ms(B).



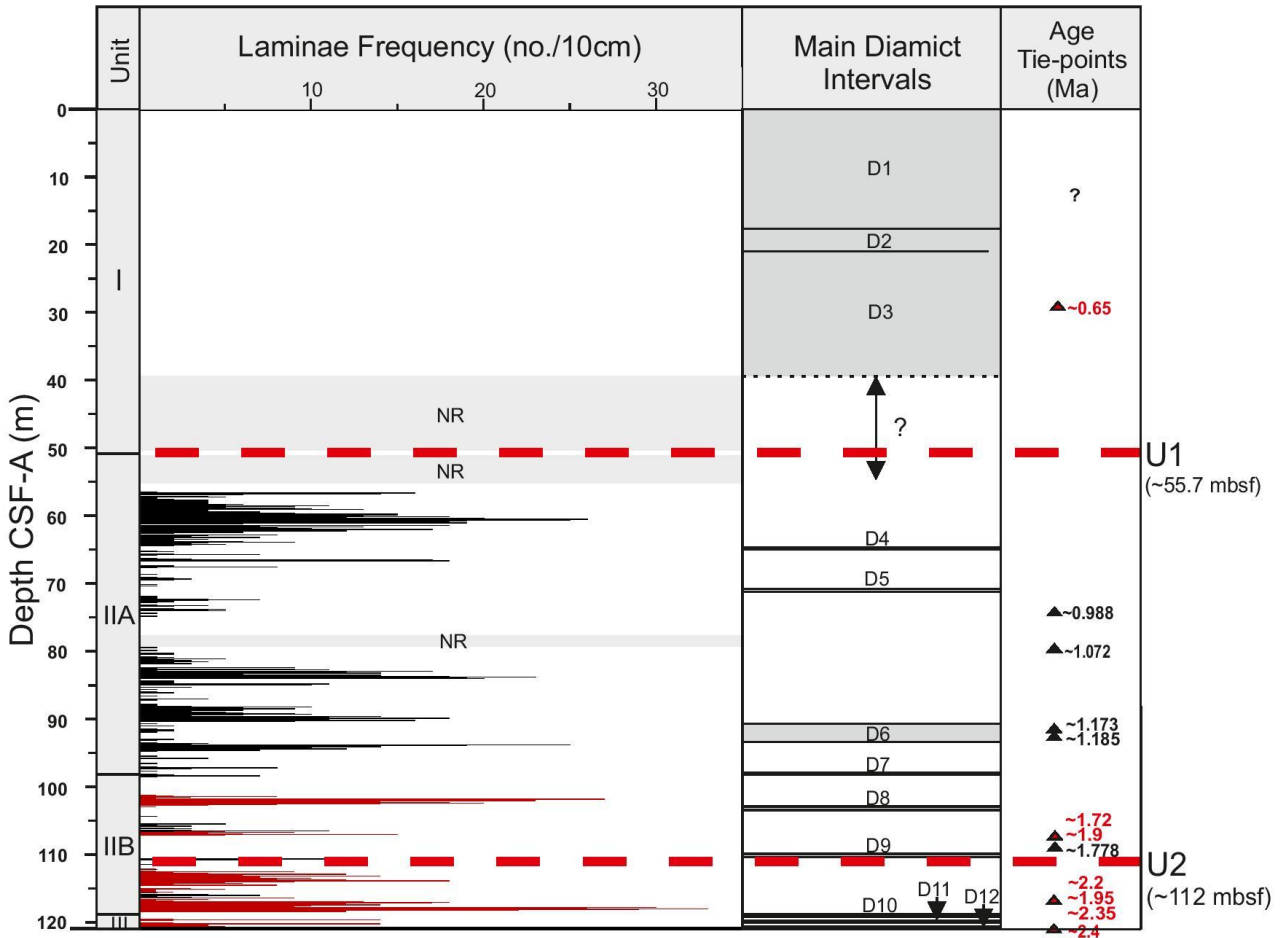
1167 **Figure 9:** Closeup images of the two styles of lamination found in U1525A where A = 'Type A'
1168 laminations (61.56-61.585 mbsf) and B = 'Type B' laminations (102.415-102.45 mbsf).



1170 **Figure 10:** Core images displaying facies MDi in Unit III from A) 118.54-118.64 mbsf and B) 119.96-
 1171 120.28 mbsf.



1172 **Figure 11:** Characteristics of sediments in Unit III including interpreted illustration of sedimentary
 1173 features and texture from Interbedded Mud and Muddy Diamict, facies MDi (118.51-118.80 mbsf)
 1174 and grain size distribution spectra for diamicts (green) and mud (orange) from all samples in facies
 1175 MDi.

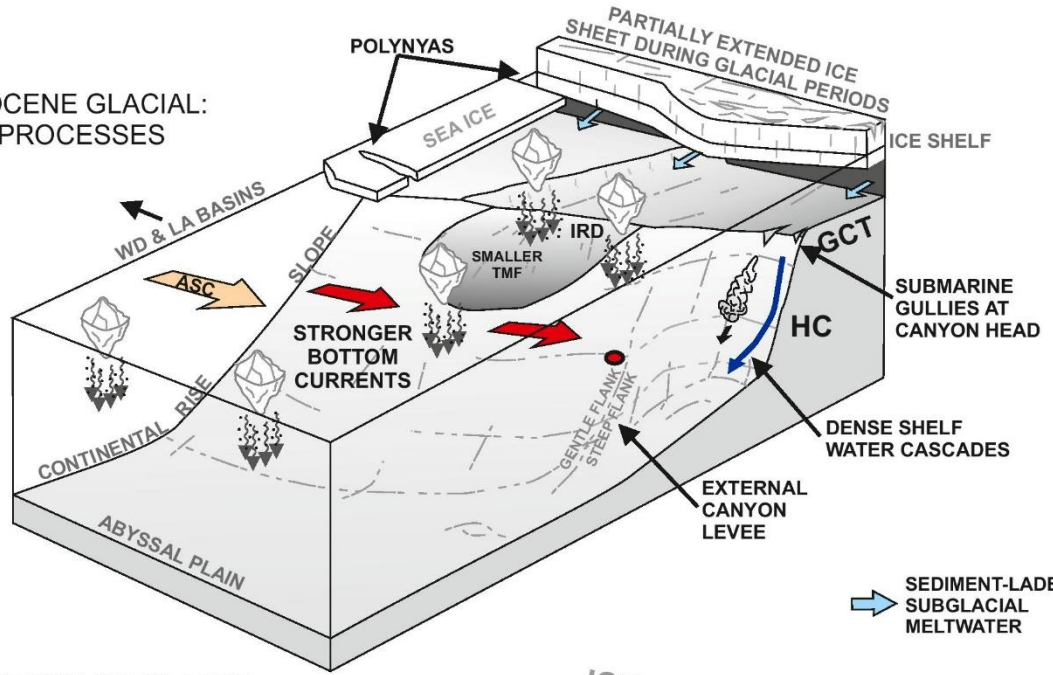


1176 **Figure 12:** Graph showing expanded view of laminae frequency against occurrence of diamict
 1177 intervals in Hole U1525A (D1-12). Type A laminae are represented by black bars. Type B laminae are
 1178 red. NR = intervals of missing sediment recovery. Thin black dashed line in main diamict interval
 1179 column reflects uncertainty over size of diamict interval due to non-recovery of sediment. Red
 1180 dashed lines show locations of chronostratigraphic unconformities interpreted in McKay et al.,
 1181 2019b (U1 and U2). Age tie-points as in figure 2.

A

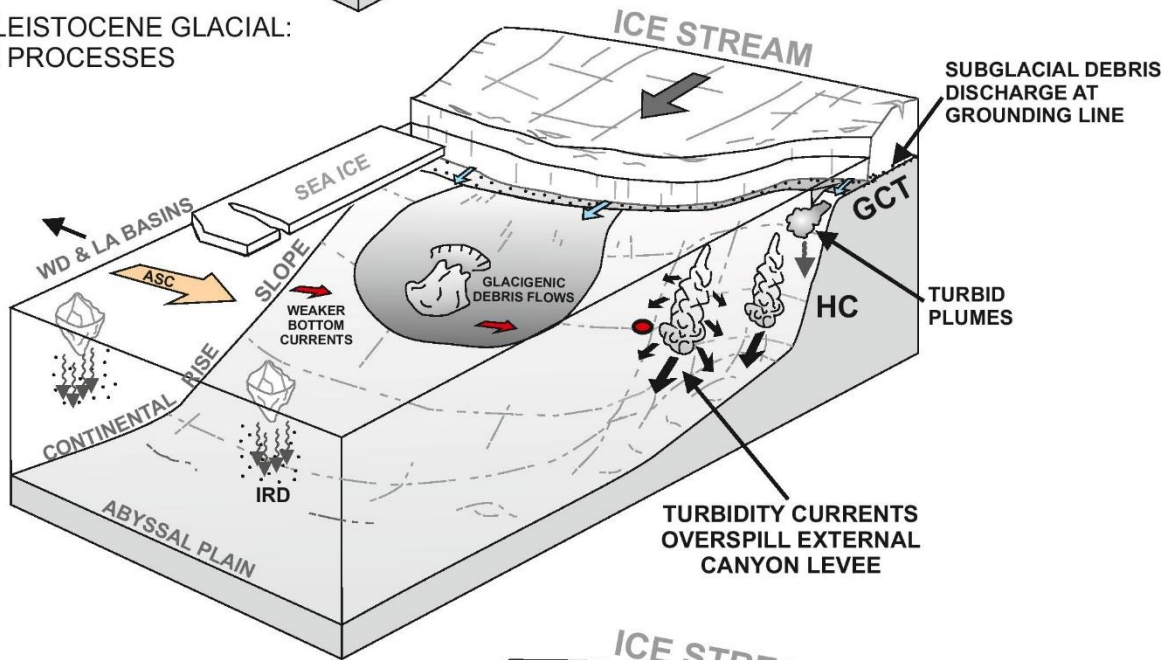
EARLY PLEISTOCENE GLACIAL:
ALONG-SLOPE PROCESSES

● U1525



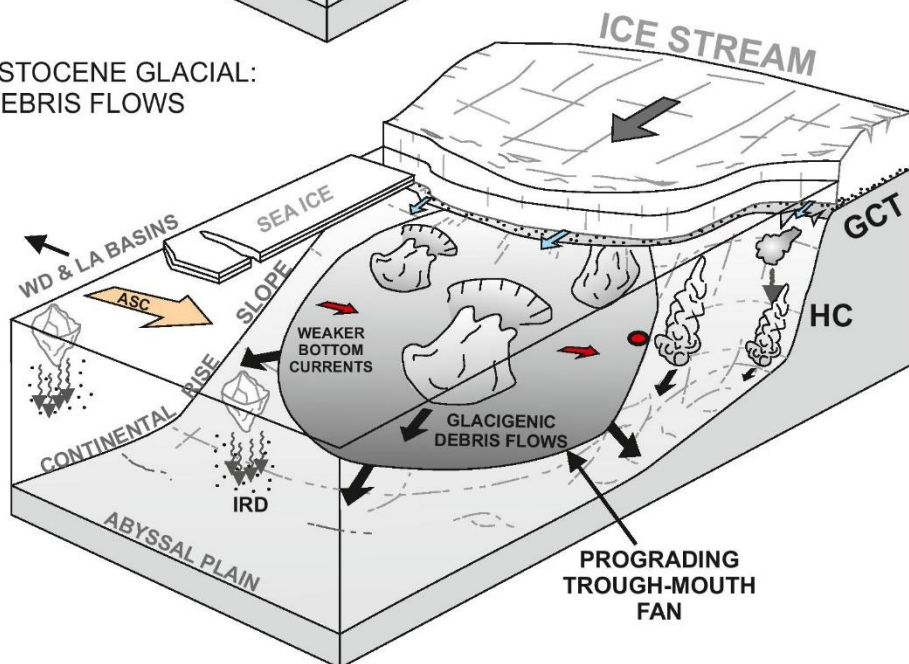
B

EARLY-MID PLEISTOCENE GLACIAL:
DOWNSLOPE PROCESSES



C

MID-LATE PLEISTOCENE GLACIAL:
GLACIGENIC DEBRIS FLOWS



1183 **Figure 13:** Conceptual diagrams showing differences between glacial period scenarios for: A) early
 1184 Pleistocene; B) early-mid Pleistocene; and C) mid-late Pleistocene. Red circle represents IODP Site
 1185 U1525. Red arrows show relative strength of bottom currents. Light blue arrows show release of
 1186 sediment-laden subglacial meltwater. ASC = Antarctic Slope Current; GCT = Glomar Challenger
 1187 Trough; HC = Hillary Canyon; TMF = Trough-mouth Fan; WD & LA = Whales Deep and Little America
 1188 Basins.

1189 **Tables**

1190 **Table 1:** Sedimentary facies observed in the top 121.05 m of Hole U1525A, based on grain size
 1191 characteristics, visual core description and physical properties. Lithostratigraphic units used follow
 1192 McKay et al., 2019. For full lithological descriptions, see Supplementary Information.

Lithostratigraphic Unit (McKay et al., 2019b)	Facies Abbreviation	Facies Name	Lithological Description	Facies Interpretation
I	MDm	Massive muddy diamict	Grey, massive, diatom-bearing diamict with occasional large dropstones and some slight bioturbation in the uppermost 10m. Matrix very poorly sorted fine sandy muds.	Debris flow deposition of subglacial or grounding-line proximal diamict from shelf. Deposited during margin-proximal glacials.
I	MDs	Stratified muddy diamict	Very stiff, dark brown to light yellowish brown, diatom-bearing, weakly-stratified diamict with very large cm-scale clasts and sharp upper (+lower?) contacts. Matrix very poorly sorted fine sandy muds.	Debris flow deposition of subglacial or grounding-line proximal diamict from shelf. Deposited during margin-proximal glacial. IRD influence?
IIA	Ms(A)	Mud with Type A silt laminae and dispersed clasts	Mode 1: Greenish-grey, strongly Type A-laminated diatom-bearing mud. Mode 2: Greenish-grey, weak to rare Type A laminated mud with rare dispersed clasts and grey cm-scale muddy diamicts with sharp upper contacts. Fine to medium silt matrix interbedded on cm to dm-scale with intervals of coarser silt/very fine sandy mud. Rare bioturbation.	Frequent low-density turbidity current deposition. Deposited during margin-proximal glacials/deglaciations Infrequent low-density turbidity current deposition. Hemipelagic suspension settling: fine-grained material + IRD rainout. Deglacial/Interglacial.

IIA/IIB	Mm	Massive mud	Greenish-grey, massive fine to medium silty muds with rare dispersed mm-scale clasts and rare bioturbation.	Hemipelagic suspension settling: fine-grained material + occasional IRD rainout. Sea ice? Interglacial.
IIA	SDi	Interbedded diatom-bearing muddy diamict/sandy mud and foraminifera-rich clast-rich sandy diamict	Light yellowish-brown foraminifera-rich muddy fine to medium sands to sandy mud with gradational contacts, interbedded on the dm-scale with faintly Type A laminated sandy-mud or muddy diamict.	Intense IRD + pelagic rainout of foraminifera (+bottom current winnowing of fine-grained material). Infrequent low-density turbidity current deposition. Interglacial (/full glacial collapse).
IIB	Ms(B)	Mud with Type B silt and gravel laminae and dispersed clasts	Mode 1: Greenish-grey, strongly Type B-laminated diatom-rich mud with dispersed clasts, and gravel layers. Infrequent slight to heavy bioturbation. Mode 2: Greenish-grey, faintly/weakly Type B-laminated diatom-rich mud with dispersed clasts, gravel layers and cm-scale diamicts. Common slight to heavy bioturbation.	Bottom current winnowing Hemipelagic suspension settling: fine-grained material + IRD rainout Sea ice? Deglacial/Interglacial Weak bottom current winnowing Hemipelagic suspension settling: fine-grained material + Sea ice? IRD rainout Distal Glaciation/Deglacial
III	MDi	Interbedded mud and muddy diamict	Greenish-grey cm-scale, diatom-rich diamict interbedded on cm to dm-scale with faintly Type B-laminated diatom-rich mud. Heavily bioturbated in places, and contains dispersed clasts/gravel layers.	Hemipelagic suspension settling: fine-grained material + intense IRD rainout Weak bottom current winnowing Distal Glaciation/Deglacial